

**SIMULATING AEROSOL FORMATION AND EFFECTS IN NO<sub>x</sub> ABSORPTION IN OXY-FIRED  
BOILER GAS PROCESSING UNITS USING ASPEN PLUS**

**by**

**DAVID DANIEL SCHMIDT**

**A THESIS**

**Submitted in partial fulfillment of the requirements for the degree**

**MASTER OF SCIENCE**

**Department of Chemical Engineering  
College of Engineering**

**KANSAS STATE UNIVERSITY  
Manhattan, Kansas**

**2013**

**Approved by:  
Major Professor  
Dr. Larry Erickson**

## **Abstract**

Oxy-fired boilers are receiving increasing focus as a potential response to reduced boiler emissions limits and greenhouse gas legislation. Among the challenges in cleaning boiler gas for sequestration is attaining the necessary purity of the CO<sub>2</sub>. A key component in the oxy-fired cleaning path is high purity SO<sub>x</sub> and NO<sub>x</sub> removal, often through absorption using the lead-chamber or similar process.

Aerosol formation has been found to be a source of product contamination in many flue gas absorption processes. A number of authors presented simulation methods to determine the formation of aerosols in gas absorption. But these methods are numerically challenging and not suitable for day-to-day analysis of live processes in the field. The goal of this study is to devise a simple and practical method to predict the potential for and effect of aerosol formation in gas absorption using information from Aspen Plus, a commonly used process simulation tool. The NO<sub>x</sub> absorber in an oxy-fired boiler CO<sub>2</sub> purification system is used as a basis for this investigation.

A comprehensive review of available data suitable for simulating NO<sub>x</sub> absorption in an oxy-fired boiler slipstream is presented. Reaction rates for eight reactions in both liquid and vapor phases are covered. These are entered into an Aspen Plus simulation using a RadFrac block for both rate-based and equilibrium reactions. A detailed description of the simulation format is given. The resulting simulation was compared to a previously published simulation and process data with good agreement.

An overall description of the aerosol formation mechanism is presented, along with an estimate of expected aerosol nuclei reaching the NO<sub>x</sub> absorption process. A method to estimate aerosol quantities produced based on inlet gas nuclei concentration and available condensable water vapor is presented.

To estimate aerosol composition and emissions, an exit gas slipstream is used to equilibrate with a pure water aerosol using an Aspen Plus Equilibrium Reactor block. Changing the composition of the initial aerosol feed liquid suggests that the location of aerosol formation may influence the final composition and emissions.

## Table of Contents

List of Figures .....	v
List of Tables .....	vii
Nomenclature .....	viii
Introduction .....	x
1 Reaction and Kinetics .....	1
1.1 Reaction Overview .....	1
1.2 Reaction Data .....	2
1.2.1 Reaction 1 $2NO + O_2 \rightarrow 2NO_2$ .....	2
1.2.2 Reaction 2 $2NO_2 \rightleftharpoons N_2O_4$ .....	3
1.2.3 Reaction 3 $NO + NO_2 + H_2O \rightleftharpoons 2HNO_2$ .....	3
1.2.4 Reaction 4 $NO + NO_2 \rightleftharpoons N_2O_3$ .....	4
1.2.5 Reaction 5 $N_2O_3 + H_2O \rightleftharpoons 2HNO_2$ .....	4
1.2.6 Reaction 6 $N_2O_4 + H_2O \rightleftharpoons HNO_2 + HNO_3$ .....	5
1.2.7 Reaction 7 $2NO_2 + H_2O \rightleftharpoons HNO_2 + HNO_3$ .....	5
1.2.8 Reaction 8 $3HNO_2 \rightleftharpoons H_2O + 2NO + HNO_3$ .....	6
2 Aspen Simulation .....	7
2.1 Diffusion Coefficients .....	7
2.2 Henry's Law Constants .....	7
2.3 Heat of Formation .....	8
2.4 Simulation Components .....	9
2.5 Property Methods and Parameters .....	9
2.6 RadFrac Parameters .....	12
2.7 Column Specifications .....	12
2.8 Reaction Kinetics .....	14
2.9 Inlet Specifications .....	16
2.10 Convergence .....	17
2.11 Validation of Simulator .....	17
2.12 Sensitivity Analysis .....	18
3 Formation of Aerosols .....	21
3.1 Definition of Aerosols .....	21
3.2 Formation Mechanisms .....	21
3.3 Particle Growth .....	25

3.4	Characterization of Particulate Nuclei .....	26
3.5	Modeling and Prediction .....	32
3.5.1	Saturation Ratio .....	32
3.5.2	Particle Size.....	34
4	Simulating Aerosol Effects on NO <sub>x</sub> Absorption.....	36
4.1	Effect of Absorption Variables on Saturation Ratio and NO <sub>x</sub> Removal.....	37
4.1.1	Inlet Gas Temperature .....	37
4.1.2	Inlet Liquid Temperature .....	40
4.1.3	Inlet Gas Flow.....	43
4.1.4	Inlet Liquid Flow.....	45
4.1.5	Liquid/Gas Temperature .....	48
4.1.6	System Pressure .....	51
5	Aerosol Effects.....	53
5.1	Availability of Condensable Vapor.....	53
5.2	Range of Estimated Aerosols.....	54
5.3	Simulating Aerosol Equilibrium.....	56
5.4	Aerosol emission estimates .....	58
6	Conclusions .....	65
7	References .....	66
8	Appendix.....	69

## List of Figures

Figure 1 - Summary of NO <sub>x</sub> liquid and gas phase reactions in water based absorption .....	1
Figure 2 – Aspen Plus RadFrac block .....	12
Figure 3 – Column packing specification .....	13
Figure 4 – RadFrac rate-based calculation parameters.....	13
Figure 5 – RadFrac mass transfer calculation methods.....	14
Figure 6 – NO <sub>x</sub> concentration column profile for base case .....	17
Figure 7 – Base simulation compared to simulation and measured data by Loutet et al.....	18
Figure 8 – Humidification of cold air by hot water: nucleation rate (J) vs. Number of Transfer Units (NTU) according to classical theory .....	24
Figure 9 – Calculated saturation profiles for different number concentration of nucleation kernels.....	25
Figure 10 – Calculated droplet diameter in the quench for different concentrations of nucleation kernels.....	26
Figure 11 – A typical coal fired power station .....	27
Figure 12– Summary of differential size distribution at the outlets of six coal fired utility boilers of various capacities and firing methods.....	28
Figure 13 – Particle size distribution after ESP.....	29
Figure 14 – Ultrafine (0.1 – 1 μm) particulate concentration in flue gas vs. flue gas O <sub>2</sub> concentration on Utah coal. ....	30
Figure 15 – Gas and liquid temperature interactions in one stage of packed absorber column.....	33
Figure 16 – Comparison of different equation methods to model saturation ratios. ....	34
Figure 17 – Maximum particle size vs. nuclei concentration from data extracted from Ehrlich and Schaber .....	35
Figure 18 – Flowsheet of calculation process for aerosols effect.....	36
Figure 19 - NO <sub>x</sub> % removal vs. inlet gas temperature.....	38
Figure 20 - Column temperature profile – 7 °C gas inlet temperature .....	38
Figure 21 - Column temperature profile – 19 °C gas inlet temperature .....	39
Figure 22 – Effect of inlet gas temperature on saturation ratio .....	39
Figure 23 - NO <sub>x</sub> % removal vs. inlet gas temperature.....	41
Figure 24 - Column temperature profile – 7 °C liquid inlet temperature .....	41
Figure 25 - Column temperature profile – 19 °C liquid inlet temperature .....	42
Figure 26 – Effect of liquid inlet temperature on saturation ratio.....	42
Figure 27 - NO <sub>x</sub> % removal vs. inlet gas flow.....	43
Figure 28a - Column temperature profile comparison at +20% gas flow.....	44

Figure 28b - Column temperature profile comparison at -20% gas flow .....	44
Figure 29 – Effect of gas flow rate on saturation ratio.....	45
Figure 30 - NO <sub>x</sub> % removal vs. inlet liquid flow .....	46
Figure 31a - Column temperature profile comparison at +15% liquid flow .....	46
Figure 31b - Column temperature profile comparison at -20% liquid flow .....	47
Figure 32 – Effect of liquid flow rate on saturation ratio .....	47
Figure 33 - % NO <sub>x</sub> removal vs. various inlet gas and liquid temperature .....	49
Figure 34 - Column temperature profile at 21/3 °C gas/liquid inlet temperature .....	50
Figure 35 - Column temperature profile at 5/19 °C gas/liquid Inlet temperature.....	50
Figure 36 – Effect of gas and liquid temperatures on saturation ratio .....	51
Figure 37 - % NO <sub>x</sub> removal vs. system pressure .....	52
Figure 38 – Effect of system pressure on saturation ratio.....	52
Figure 39 – Highlighted area on column saturation ratio profile showing areas where <i>S &gt; Scrit</i> .....	53
Figure 40 - Aerosol mass flow vs. entering nuclei concentration. ....	55
Figure 41 – Addition to Aspen NO <sub>x</sub> absorber model to calculate equilibrium concentrations in aerosols.....	57
Figure 42 - Aerosol dissolved gas component mole fraction.....	58
Figure 43 - Components dissolved in aerosol in base case.....	60
Figure 44 – Total nitrogen compounds emitted with aerosols at various absorber conditions....	62
Figure 45 – Total nitrogen compounds emitted with aerosol in contaminated water case vs. base and 21-3 cases. ....	64
Figure A.1 – Stage temperature data in Aspen .....	70
Figure A.2 – Stage composition data in Aspen.....	71
Figure A.3 – Aspen binary property input screen.....	72
Figure A.4 – Vapor pressure data in Aspen.....	72
Figure A.5 – Excel spreadsheet showing example calculations for saturation ratio .....	73
Figure A.6 – Excel spreadsheet showing available vapor calculations .....	75

## List of Tables

Table 1 – Heat of formation data of selected compounds from Perry .....	8
Table 2 – Compounds modeled as Henry’s law components in Aspen simulation.....	9
Table 3 – Aspen global property specifications .....	10
Table 4a – Henry’s law constant values used in Aspen simulation.....	11
Table 4b – Henry’s law constant values used in Aspen simulation.....	11
Table 5 - Reaction kinetic specifications in Aspen Plus .....	15
Table 6 - Inlet Feed gas composition .....	16
Table 7 – Kinetic constants and equilibrium coefficients used for sensitivity analysis .....	19
Table 8 – Simulation sensitivity to changes in kinetic parameters .....	20
Table 9 – Typical particle size of aerosols.....	21
Table 10 – Composition of particulate (%w) after WFGD .....	29
Table 11 – Data used for calculation of nuclei to GPU NO <sub>x</sub> absorption process .....	31
Table 12 – Calculated particle properties .....	31
Table 13 – Simulated liquid / gas inlet temperature combinations .....	48
Table 14 – Total water available for aerosol condensation above <i>Scrit</i> at 21 °C gas inlet and 3 °C liquid inlet temperatures.....	54
Table 15 – Range of particle concentrations for simulation .....	56
Table 16 – Component categories in aerosol liquid.....	59
Table 17 – Base case simulation results .....	61
Table 18 – Water feed composition used in 21-3 contaminated water case simulation .....	63

## Nomenclature

<u>Term</u>	<u>Description</u>	<u>Units</u>
$C_N$	Concentration of particles	$\frac{\text{number of particles}}{m^3}$
$d$	Diameter	$\mu m$
$D_x$	Diffusion coefficient for component x	$\frac{m^2}{s}$
GPU	Gas processing unit	NA
$H_x$	Henry's law constant for component x	$\frac{mol}{l \cdot atm}$
$\Delta H_x$	Heat of reaction for reaction x	$\frac{kJ}{mole}$
$J$	Nucleation rate	$\frac{1}{m^3 s}$
$K_{eq(x)}$	Equilibrium coefficient for reaction x	$\frac{m^3}{kmole}$ or as noted
k	Reaction rate kinetic coefficient	NA
L/G	Ratio of liquid to gas mass flow	dimensionless
$l$	Volume	liter
NTU	Number of transfer units	dimensionless
$p_i$	partial pressure of component i	Atm
$p_i^{eq}$	equilibrium partial pressure of component i	Atm
$Q$	Mass flow	$\frac{kg}{hr}$
$r_x$	Reaction rate for reaction x	$\frac{mol}{l \cdot s}$



<u>Term</u>	<u>Description</u>	<u>Units</u>
$S$	Saturation ratio	dimensionless
$T$	Temperature	$^{\circ}K$
$V$	Volume	$\mu m^3$
$v$	Volumetric flow	$\frac{l}{min}$
[xx]	Concentration of component xx	$\frac{moles}{l}$
$y_i$	Gas phase mole fraction of component i	NA

Subscripts

$a$	aerosol property	NA
drop	droplet property	NA
$g$	gas phase	NA
$i$	condensing component	NA
$l$	liquid phase	NA
$n$	absorber stage number in Aspen simulation	NA

Greek

$\rho$	density	$\frac{g}{cm^3}$
--------	---------	------------------

## Introduction

Compared to conventional air fired boilers, oxy-fired boilers create less total SO<sub>2</sub> and NO<sub>x</sub> compounds. But due to the decreased total volume of flue gas with the reduction of N<sub>2</sub> in the combustion gas, the concentration of SO<sub>2</sub> and NO<sub>x</sub> can be greater in the gas phase than in conventional boilers. For CO<sub>2</sub> recovery for sequestration or enhanced oil recovery, the required levels of non-CO<sub>2</sub> gases in the condensed CO<sub>2</sub> stream may be <5%. To attain these levels of purity, the oxy-fuel produced flue gas must be treated to remove SO<sub>2</sub> and NO<sub>x</sub> contaminants. A potential pitfall in attaining these high levels of purity is the effect of aerosol formation and the ability of aerosols to transport contaminants out of the absorption process as a liquid suspended in the gas phase.

Aqueous aerosols are recognized as a potential problem in many washing and cleaning processes, including flue gas scrubbing as has been practiced commercially for many years. Aerosols can be expected to transport dust and absorption material out of the processes, and potentially into the downstream atmosphere or product. Traditionally, absorption processes were equipped with liquid-gas separation devices on the outlet, such as chevron baffles or mesh mist eliminators, with the expectation that these mechanisms would eliminate any significant loss of entrained liquids out of the discharge of the process.

Some examples of problems encountered from the aerosol formation in absorption processes include:

- High pH aerosols formed in flue gas desulfurization units that are not captured by existing mist eliminators and end up in a CO<sub>2</sub> capture column further downstream.
- High ammonium sulfate emissions downstream of an ammonia vapor scrubber, resulting in higher nitrogen emissions from the stack.
- Unaccounted amine losses for CO<sub>2</sub> capture systems caused by aerosols transporting dissolved amine into the water wash process or stack.

- Contaminated CO<sub>2</sub> product streams caused by aerosols transporting absorbent with the CO<sub>2</sub> product gas.

But little data exists that quantifies the potential effect of aerosols on similar CO<sub>2</sub> cleaning processes.

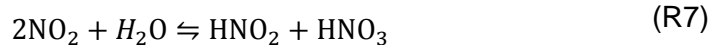
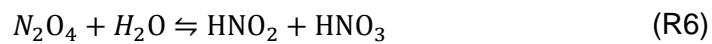
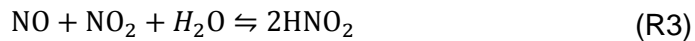
This work focuses on the reduction of NO<sub>x</sub> compounds after initial desulfurization. Due to the relatively high temperatures, NO<sub>x</sub> compounds in the flue gas from oxy-fired boilers are mainly in the form of NO [1]. Depending on the mechanism for desulfurization of the flue gas, the primary species entering the NO<sub>x</sub> removal column may be either NO or NO<sub>2</sub> [2].

Aerosols are not captured in the typical gas sampling and analysis equipment used for most environmental modeling and testing, and aerosols were therefore often ignored. However, more detailed testing using equipment specifically designed for capturing fine entrained liquids shows that aerosols are far too fine to be captured by traditional coarse separation devices. Particles in the 0.4 – 4 μm size range can hardly be removed by inertial separators [3]. Under certain conditions and processes aerosols can exist in concentrations high enough to cause significant escape of pollutants to the environment [4].

# 1 Reaction and Kinetics

## 1.1 Reaction Overview

The reactions of primary interest for modeling NO<sub>x</sub> absorption by water in an oxygen containing atmosphere are listed below. See the notation section for descriptions of nomenclature [5].



Reactions take place primarily in the bulk gas phase and liquid film as shown graphically in Figure 1.

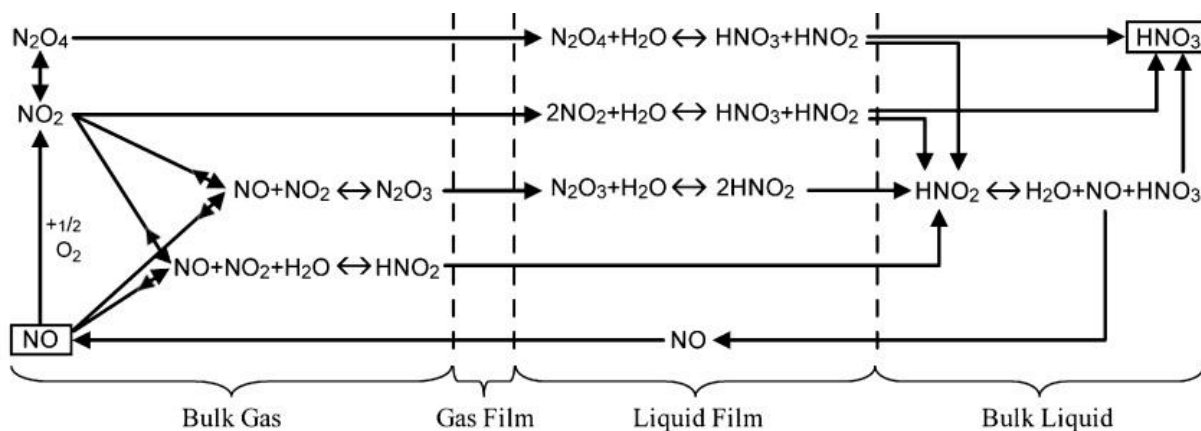
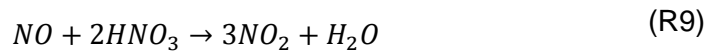


Figure 1 - Summary of NO<sub>x</sub> liquid and gas phase reactions in water based absorption [6]

At lower liquid phase nitric acid concentrations (< 30%) the rate determining step is reaction R1 since  $NO_2$  has roughly an order of magnitude better absorption than  $NO$  [7].

Reaction 1 is assumed to be irreversible at temperatures below  $350^{\circ}C$ . The remaining gas phase reactions of  $NO$  are essentially instantaneous, and absorption of products  $N_2O_4$ ,  $N_2O_3$ ,  $HNO_2$ , &  $HNO_3$  generally increases with increasing molecular weight [8].

For absorption of the  $NO_2$  gas, absorption is controlled by reactions of  $NO_2$  with the bulk liquid, and gas side mass transfer resistance is generally considered to be insignificant. However, at high liquid phase nitric acid concentrations (>60%) the vapor pressure of  $HNO_3$  is significant. In that case, gas film reactions are more likely to occur, including direct reaction with  $NO$  from reaction R9 [7].



$NO_x$  absorption is an important process for both nitric acid production and pollution control and has been extensively studied over the years. But published kinetic data for some reactions can vary widely between different sources.

## 1.2 Reaction Data

### 1.2.1 Reaction 1 $2NO + O_2 \rightarrow 2NO_2$

In an oxygenated gaseous environment, the reaction is 3<sup>rd</sup> order [8] when the partial pressure of  $NO > 0.8$  mm Hg. There are other published reaction rates, but they tend to be older data arrived at using higher  $NO$  concentrations [7].

$$r_1 = (1.2 \times 10^3) e^{\left(\frac{530}{T}\right)} [NO]^2 [O_2] \quad (1)[8]$$

$$\Delta H_{r1} = -1127 \text{ kJ/mol} \quad (2)[9]$$

$$\Delta H_{r1} = -5.7 \times 10^{-10} \text{ kJ/mol} \quad (3)[10]$$

$$\Delta H_{r1} = -113 \text{ kJ/mol} \quad (4)[11]$$

$$\Delta H_{r1} = -51.1 \text{ kJ}/(\text{mol } NO_2) \quad (5)[12]$$

Although reaction 1 is reversible, most authors ignore the reverse reaction R10 at temperatures below 360°C. Equation 6 gives the rate expression for the reverse reaction. However, it can be removed from the simulation at low temperatures.



$$r_{10} = 9.6592 \times 10^{11} e^{(-22380/T)} [NO_2]^2 \quad (6)[13]$$

$$\Delta H_{r10} = 57.1 \text{ kJ}/\text{mol} \quad (7)[12]$$

A significant difference exists between heat of reaction listed in the literature, primarily from Thiemann [9], Suchak [10] and Patwardhan [11]. For consistency, data from Thiemann is presented in the remainder of this paper when data from that author is available, along with heat of reaction calculated from heat of formation data in Perry's Handbook [12].

### 1.2.2 Reaction 2 $2NO_2 \rightleftharpoons N_2O_4$

$$K_{eq(r2)} = 7.572 \times 10^4 \frac{\text{m}^3}{\text{kmol}} \quad (8)[13]$$

$$\Delta H_{r2} = -57.2 \text{ kJ}/\text{mol} \quad (9)[9]$$

$$\Delta H_{r2} = -57.32 \text{ kJ}/(\text{mol } N_2O_4) \quad (10)[12]$$

### 1.2.3 Reaction 3 $NO + NO_2 + H_2O \rightleftharpoons 2HNO_2$

$$K_{eq(r3)} = 1.85 \times 10^{-12} e^{\frac{4723}{T}} \left( \frac{1}{\text{Pa}} \right) \quad (11)[14]$$

$$\Delta H_{r3} = -2.05 \times 10^{-10} \text{ kJ}/\text{mol} \quad (12)[10]$$

$$\Delta H_{r3} = +10.26 \text{ kJ}/(\text{mol } HNO_2) \quad (13)[12]$$

Due to low solubility of NO in water, reaction R3 is expected to take place primarily in the humid gas phase or the gas film layer. However, Siddiqi also reported the water phase reaction rate as:

$$r_{3(aq)} = (5.41 \times 10^6) [NO_2] [NO] \quad (14)[15]$$

#### 1.2.4 Reaction 4 $NO + NO_2 \rightleftharpoons N_2O_3$

$$r_4 = 4.75 \times 10^{12} \left( [NO][NO_2] - \frac{[N_2O_3]}{\left( 65.3 \times 10^{-9} e^{\left( \frac{4740}{T} \right)} \right) (RT)} \right) \quad (15)[2]$$

$$K_{eq(r4)} = 2.156 \times 10^{-2} \frac{m^3}{mol} \quad (16)[13]$$

$$\Delta H_{r4} = -40 \text{ kJ/mol} \quad (17)[9]$$

$$\Delta H_{r4} = -39.98 \text{ kJ}/(\text{mol } N_2O_3) \quad (18)[12]$$

#### 1.2.5 Reaction 5 $N_2O_3 + H_2O \rightleftharpoons 2HNO_2$

$$r_5 = (10^{4.23044}) [N_2O_3] \quad (19)[18]$$

$$\Delta H_{r5} = -3.99 \times 10^{-7} \text{ kJ/kmol} \quad (20)[10]$$

$$\Delta H_{r5} = +30.25 \text{ kJ}/(\text{mol } HNO_2) \quad (21)[12]$$

Although no temperature dependence was found for the reaction rate constant, the creation of  $N_2O_3$  is the rate controlling step, so this reaction is particularly insensitive to the reaction rate.

### 1.2.6 Reaction 6 $N_2O_4 + H_2O \rightleftharpoons HNO_2 + HNO_3$

$$r_6 = \left(10^{\left(\frac{-4139}{T} + 16.3415\right)}\right) [N_2O_4] \quad (22)[9]$$

$$\Delta H_{r6} = -87.0 \text{ kJ/mol} \quad (23)[9]$$

$$\Delta H_{r6} = -58.2 \text{ kJ/(mol } HNO_3) \quad (24)[12]$$

### 1.2.7 Reaction 7 $2NO_2 + H_2O \rightleftharpoons HNO_2 + HNO_3$

Reaction 7 is considered a vapor phase or film reaction by some authors and liquid phase by others.

England [19] determined that reaction 7 was the overall reaction that resulted in  $HNO_3$  in the vapor phase, with the rate described by equation 25. The reaction can form nitric acid in mist form, which can either be further absorbed by the liquid phase or transported out of the absorber in the gas phase. The reaction rate is dependent on both  $NO_2$  concentration and gas phase relative humidity.

$$r_7 = [-2k_1[NO_2]^2[H_2O] + 2k_2[HNO_3][HNO_2]] \quad (25)[19]$$

$$k_1 = 5.5 \times 10^4 e^{\frac{-978}{RT}} \quad (26)$$

$$k_1 = 5.85 \times 10^3 e^{\frac{-978}{RT}} \quad (27)$$

The liquid phase reaction is limited by the absorption rate of  $NO_2$ , suggesting the importance of accurate Henry's law coefficients for  $NO_2$ .

$$r_7 = 10^{4.67209} [NO_2]^2 \quad (28)[18]$$

$$\Delta H_{r7} = -5.36 \times 10^{-7} \text{ kJ/kmol} \quad (29)[10]$$



$$\Delta H_{r7} = -115.52 \text{ kJ}/(\text{mol } HNO_3) \quad (30)[12]$$

**1.2.8 Reaction 8**  $3HNO_2 \rightleftharpoons H_2O + 2NO + HNO_3$

$$r_8 = 10^{\left(\frac{-6200}{T} + 20.1979\right)} \left( \frac{[HNO_2]^4}{[NO]^2[HNO]^2} \right) \quad (31)[9]$$

$$\Delta H_{r8} = -15.3 \text{ kJ}/\text{mol} \quad (32)[9]$$

$$\Delta H_{r8} = +59.56 \text{ kJ}/(\text{mol } HNO_3) \quad (33)[12]$$

## 2 Aspen Simulation

The reaction data in Chapter 1 was used to build a working model of NO<sub>x</sub> absorption in Aspen Plus. Aspen was selected because it is one of the most commonly used simulation tools in industry and it is robust enough to be used in field applications to predict operating performance based on actual operating data. The following sections detail the parameters and methods used to produce the simulation.

### 2.1 Diffusion Coefficients

In the liquid phase in electrolyte solutions, the Nernst-Hartley equation can be used to estimate effective diffusion coefficients in dilute solutions [20]. Kenig [20] suggests that gas diffusion coefficients for NO<sub>x</sub> absorption can be accurately predicted using the Chapman-Enskog-Wilke-Lee model, which is available in Aspen. However, Aspen suggests that this model is primarily applicable for low pressure gases, so the Dawson-Khoury-Kobayashi model was used.

### 2.2 Henry's Law Constants

Henry's constants are taken from a compilation by Sanders [22] with T<sub>0</sub> = 298.15 °K. Considerable variation exists among published data for some species. Published values of Henry's constant follow:

$$H_{NO} = (1.9 \times 10^{-3}) e^{\left(\frac{-1500}{T}\right)} \quad (34)$$

$$H_{NO_2} = (7.0 \times 10^{-3}) e^{\left(\frac{-2150}{T}\right)} \quad (35)$$

$$H_{N_2O_3} = (2.6 \times 10^1) \quad (36)$$

$$H_{N_2} = (6.1 \times 10^{-4}) e^{\left(\frac{-1300}{T}\right)} \quad (37)$$

$$H_{HNO_2} = (4.9 \times 10^1) e^{\left(\frac{-4900}{T}\right)} \quad (38)$$

$$H_{HNO_3} = (2.1 \times 10^5) e^{\left(\frac{-8700}{T}\right)} \quad (39)$$

$$H_{N_2O} = (2.4 \times 10^{-2}) e^{\left(\frac{-2600}{T}\right)} \quad (40)$$

$$H_{N_2} = (6.5 \times 10^{-4}) e^{\left(\frac{-1300}{T}\right)} \quad (41)$$

$$H_{O_2} = (1.3 \times 10^{-3}) e^{\left(\frac{-1700}{T}\right)} \quad (42)$$

### 2.3 Heat of Formation

The following heats of formation numbers were readily available in the literature (298.15 °K, 1 atm) [12].

<u>Compound</u>	<u><math>\Delta H_f</math> cal/mole</u>
NO <sub>2</sub> (g)	7960
N <sub>2</sub> O <sub>3</sub> (g)	20010
N <sub>2</sub> O <sub>4</sub> (g)	2230
HNO <sub>2</sub> (l)	-11670
HNO <sub>3</sub> (l)	-31990

*Table 1 – Heat of formation data of selected compounds from Perry*

## 2.4 Simulation Components

<u>Formula</u>	<u>Common Name</u>	<u>Henry's Component</u>
CO <sub>2</sub>	CARBON DIOXIDE	X
CO	CARBON MONOXIDE	X
H <sub>2</sub> O	WATER	
O <sub>2</sub>	OXYGEN	X
AR	ARGON	X
N <sub>2</sub>	NITROGEN	X
SO <sub>2</sub>	SULFUR-DIOXIDE	X
SO <sub>3</sub>	SULFUR-TRIOXIDE	X
HCL	HYDROGEN-CHLORIDE	X
NO	NITRIC-OXIDE	X
HNO <sub>3</sub>	NITRIC-ACID	X
HNO <sub>2</sub>	NITROUS-ACID	X
H <sub>2</sub> SO <sub>4</sub>	SULFURIC-ACID	
N <sub>2</sub> O <sub>3</sub>	NITROGEN-TRIOXIDE	X
N <sub>2</sub> O <sub>4</sub>	NITROGEN-TETROXIDE	X
NO <sub>2</sub>	NITROGEN-DIOXIDE	X
N <sub>2</sub> O	NITROUS-OXIDE	X

Table 2 – Compounds modeled as Henry's law components in Aspen simulation

## 2.5 Property Methods and Parameters

ELECNRTL was used as the Aspen property method. ELECNRTL is a versatile property method suitable for both high and low concentrations up to medium pressures. It allows the use of Henry's law coefficients for modeling solubility.

Other model specifications are shown in Tables 3 to 4b. No parameters are estimated by Aspen.

Property methods & models		Property method:	
Process type:	CHEMICAL	ELECNRTL	.....
Base method:	ELECNRTL	<input type="checkbox"/> Modify property models	
Henry components:	HC-1	Vapor EOS:	ESRK
Petroleum calculation options		Data set:	1
Free-water method:	STEAM-TA	Liquid gamma:	GMENRTL
Water solubility:	3	Data set:	1
Electrolyte calculation options		Liquid enthalpy:	HLMXELC
Chemistry ID:		Liquid volume:	VLMXELC
<input checked="" type="checkbox"/> Use true-components		<input type="checkbox"/> Heat of mixing	
		<input checked="" type="checkbox"/> Poynting correction	
		<input type="checkbox"/> Use liq. reference-state enthalpy	

Table 3 – Aspen global property specifications

When available Aspen calculated Henry's law constants were replaced with user entered values taken from published literature listed in equation 34 - 42. Table 4 lists the Henry's law constants used for all Henry's components listed in Table 2, including the Aspen source when published sources were not available. Henry's constants for  $N_2O_4$  were not available in the literature or Aspen so the coefficients for  $N_2O_3$  were used.

Temperature-dependent binary parameters								
Component i	CO	O2	N2	SO2	NO	AR	HCL	N2O
Component j	H2O	H2O	H2O	H2O	H2O	H2O	H2O	H2O
Temperature units:	C	K	K	F	K	F	F	K
Source	APV71 BINARY	USER	USER	APV71 BINARY	USER	APV71 BINARY	APV71 BINARY	USER
AIJ	174.4494834	16.36	15.7750	17.90421223	15.1420	185.8212858	-49.78140336	16.4629
BIJ	-8296.750000	-1700	-1300	-5171.327959	-1500	-14646.83388	2186.999983	-2600.0
CIJ	-23.33720000	0.0	0.0	-3028800000	0.0	-23.25470000	8.370700000	0.0
DIJ	0.0	0.0	0.0	0.0	0.0	1.70198335E-3	-5.3294445E-3	0.0
TLOWER	-1.500000000	0.0	0.0	49.73000360	0.0	33.53000373	-3.999995968	0.0
TUPPER	79.85000000	2000.000	2000.000	235.1300021	2000.000	164.9300027	68.00000346	2000.000
EIJ	0.0	0.0	0.0	0.0	0.0	0.0	0.0	0.0
Property units:	psia	atm	atm	psia	atm	psia	psia	atm

Table 4a – Henry’s law constant values used in Aspen simulation, including both literature (equation 34-42) and Aspen generated values

Temperature-dependent binary parameters								
Component i	N2O	NO2	N2O3	HNO2	HNO3	N2O4	CO2	
Component j	H2O	H2O	H2O	H2O	H2O	H2O	H2O	
Temperature units:	K	K	K	K	K	K	F	
Source	USER	USER	USER	USER	USER	USER	APV71 BINARY	
AIJ	16.4629	13.4314	0.7547	16.5556	20.9379	.7547	175.2762325	
BIJ	-2600.0	-1800	0.0	-4900.0	-8700.0	0.0	-15734.78987	
CIJ	0.0	0.0	0.0	0.0	0.0	0.0	-21.66900000	
DIJ	0.0	0.0	0.0	0.0	0.0	0.0	6.12550005E-4	
TLOWER	0.0	0.0	0.0	0.0	0.0	0.0	31.73000375	
TUPPER	2000.000	2000.000	2000.000	2000.000	2000.000	2000.000	175.7300026	
EIJ	0.0	0.0	0.0	0.0	0.0	0.0	0.0	
Property units:	atm	atm	atm	atm	atm	atm	psia	

Table 4b – Henry’s law constant values used in Aspen simulation, including both literature (equation 34-42) and Aspen generated values

Heat of formation numbers available in the literature (Table 1) were adjusted in Aspen Properties-Pure Components-Review1-DHFORM.

Aspen vapor pressure for  $\text{HNO}_2$  was not available in Aspen property parameter PLXANT-1. The Aspen calculated values for  $\text{HNO}_3$  were duplicated for  $\text{HNO}_2$ .

## 2.6 RadFrac Parameters

A simple Aspen RadFrac block was constructed as shown in Figure 2 to model an  $\text{NO}_x$  absorption column.

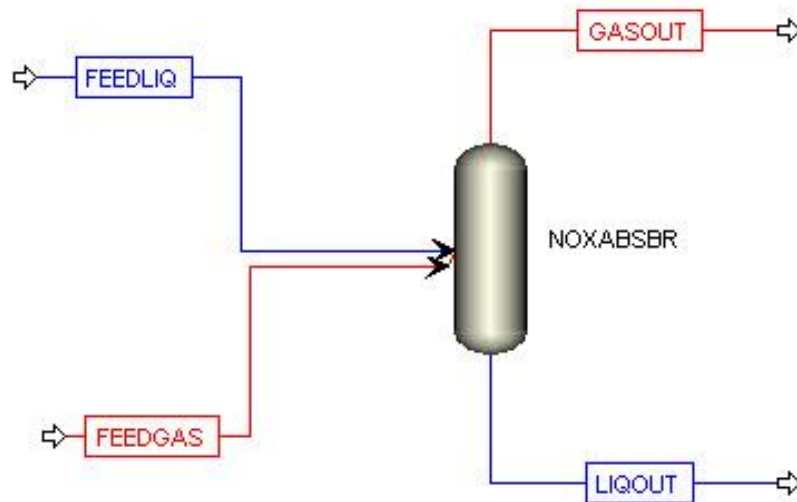


Figure 2 – Aspen Plus RadFrac block

The absorber was modeled with 35 stages, with gas in and liquid out at stage 35, liquid in and gas out at stage 1. Simulation pressure was 34.7 atm with no pressure drop across the column calculated.

## 2.7 Column Specifications

Figures 3 - 5 show the packing specifications and related estimation and calculation methods used.

Packing section						
Starting stage:	2	Ending stage:	34	Type:	MELLAPAK	
Packing characteristics						
Vendor:	SULZER	Section diameter:	3		meter	
Material:	STANDARD	Packing size:			ft	
Dimension:	250Y	Packing factor:			1/ft	
Packed height						
<input type="radio"/>	Packed height per stage:				1	cm
<input checked="" type="radio"/>	Section packed height:				8	meter

Figure 3 – Column packing specification

<input checked="" type="checkbox"/>	Rate-based calculations		
Calculation parameters			
Flow model:	Mixed		
Interfacial area factor:	1		
Heat transfer factor:	1		
Film resistance			
Liquid phase:	Filmrxn	Vapor phase:	Filmrxn
Film non-ideality correction			
Liquid phase:	No	Vapor phase:	No

Figure 4 – RadFrac rate-based calculation parameters



Mass transfer coefficient method			
Correlation:	Bravo et al. (1985)		
Heat transfer coefficient method			
Correlation:	Chilton and Colburn		
Interfacial area method			
Correlation:	Bravo et al. (1985)		
Mass transfer correlation parameter			
Critical surface tension:	75	dyne/cm	
Billet and Schultes CL:	1	Billet and Schultes CV:	1

Figure 5 – RadFrac mass transfer calculation methods

## 2.8 Reaction Kinetics

The reactions and kinetic parameters shown in Table 5 were included in the RadFrac reaction set R-1. All reactions are specified to take place in column sections 2 to 34.

Liquid holdup is specified as 1 m<sup>3</sup> in each column section. Vapor residence time is specified at 0.47 sec in all sections. Vapor holdup and liquid residence times were not specified.

Reaction #	Reaction	Type	k or $K_{eq}$	E (J/kmol)	phase	$C_i$ basis	Stoichiometry (exponents)
1	$2NO + O_2 \rightarrow 2NO_2$	kinetic	$1.2 \times 10^3$	-4406	vapor	molarity	$[NO]^2[O_2]^1$
2	$2NO_2 \rightleftharpoons N_2O_4$	equilibrium	A=11.2348	NA	vapor	molarity	NA
3	$NO + NO_2 + H_2O \rightleftharpoons 2HNO_2$	equilibrium	A=-27.0158, B=4723	NA	vapor	partial pres.	NA
4	$N_2O_3 \rightarrow NO + NO_2$	kinetic	$2.3248 \times 10^{-12}$	$3.69857 \times 10^7$	vapor	molarity	$[N_2O_3]^1$
5	$NO + NO_2 \rightarrow N_2O_3$	kinetic	$4.75 \times 10^{12}$	0	vapor	molarity	$[NO]^1[NO_2]^1$
6	$N_2O_3 + H_2O \rightarrow 2HNO_2$	kinetic	$1.6997 \times 10^4$	0	liquid	molarity	$[N_2O_3]^1[H_2O]^0$
7	$N_2O_4 + H_2O \rightarrow HNO_2 + HNO_3$	kinetic	$2.1953 \times 10^{16}$	$7.67415 \times 10^7$	liquid	molarity	$[N_2O_4]^1[H_2O]^0$
8	$2NO_2 + H_2O \rightarrow HNO_2 + HNO_3$	kinetic	$4.6991 \times 10^7$	0	liquid	molarity	$[NO_2]^2[H_2O]^0$
9	$2NO_2 + H_2O \rightarrow HNO_2 + HNO_3$	kinetic	$1.1 \times 10^5$	$4.0947 \times 10^6$	vapor	molarity	$[NO_2]^2[H_2O]^1$
10	$HNO_2 + HNO_3 \rightarrow 2NO_2 + H_2O$	kinetic	$1.17 \times 10^4$	$4.0947 \times 10^6$	vapor	molarity	$[HNO_3]^1[HNO_2]^1$
11	$3HNO_2 \rightarrow H_2O + 2NO + HNO_3$	kinetic	$2.2394 \times 10^{22}$	$1.007989 \times 10^8$	liquid	molarity	$[HNO_2]^4[NO]^{-2}$
12	$2NO_2 \rightarrow 2NO + O_2$	kinetic	$9.6592 \times 10^{11}$	$1.8607 \times 10^8$	vapor	molarity	$[NO_2]^2$
13	$NO + NO_2 + H_2O \rightarrow 2HNO_2$	kinetic	$5.41 \times 10^6$	0	liquid	molarity	$[NO]^1[NO_2]^1[H_2O]^0$

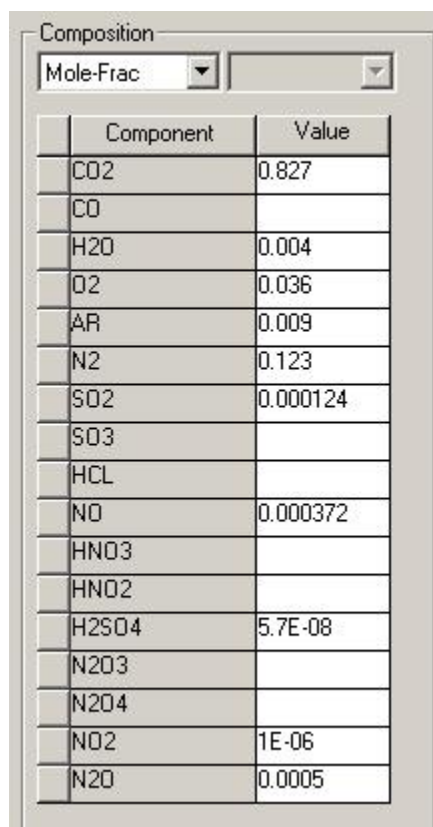
Table 5 - Reaction kinetic specifications in Aspen Plus

## 2.9 Inlet Specifications

Modeled flue gas flow was 292,107 kg/hr = 66.5 m<sup>3</sup>/min. Inlet conditions for both liquid and vapor phases for the base simulation was 34.7 atm and 13°C.

Inlet gas composition for the base model is shown in Table 6. The inlet gas composition was based on estimated inlet gas composition entering an NO<sub>x</sub> absorption stage in an oxy-fired boiler after Lead Chamber Process SO<sub>x</sub> absorption. Therefore, the feed stream contains primarily CO<sub>2</sub> and N<sub>2</sub>, with minimal contamination by sulfur compounds. No sulfur compound reactions were included in the reaction set.

For the base simulation, liquid flow was assumed to be constant at 1.0 Liquid/Gas mass ratio and composed of a 40 mole percent nitric acid solution.



Component	Value
CO2	0.827
CO	
H2O	0.004
O2	0.036
AR	0.009
N2	0.123
SO2	0.000124
SO3	
HCL	
NO	0.000372
HNO3	
HNO2	
H2SO4	5.7E-08
N2O3	
N2O4	
NO2	1E-06
N2O	0.0005

Table 6 - Inlet Feed gas composition

## 2.10 Convergence

Aspen default convergence parameters were used, except rate-based convergence tolerance was increased to  $1 \times 10^{-4}$ .

## 2.11 Validation of Simulator

Figure 7 shows the  $\text{NO}_x$  concentration profile through the absorber column. At initial conditions,  $\text{NO}_x$  removal is 81.79% mol.

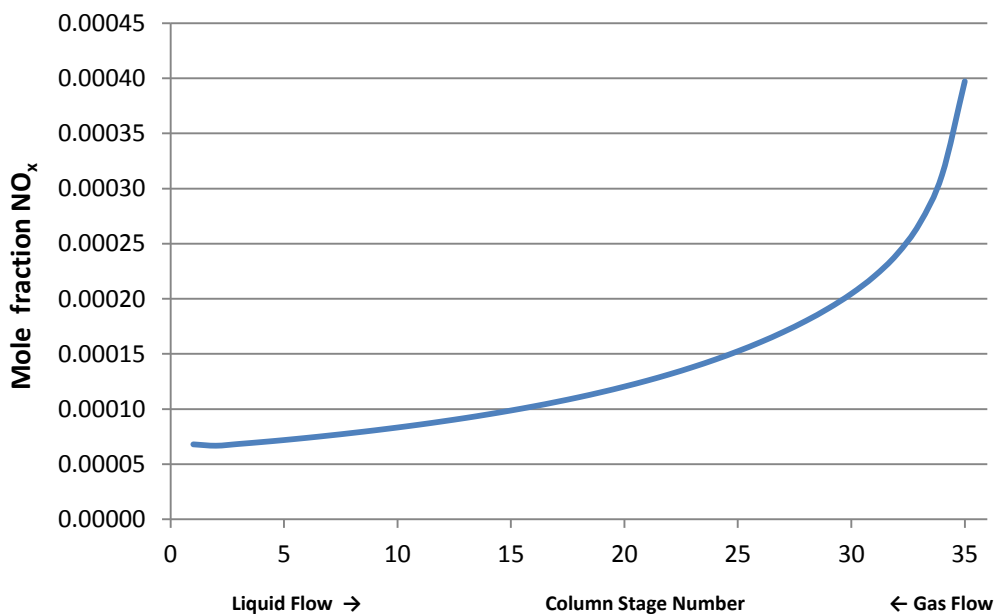


Figure 6 –  $\text{NO}_x$  concentration column profile for base case

Loutet et al. [23] constructed and validated a simulation on an existing commercial  $\text{NO}_x$  absorption tower used for the production of nitric acid. Their simulation was designed with a two stage absorber with concentrated acid circulating in the bottom section and pure demineralized water in the upper absorption section. In addition, the Loutet simulation was at considerably lower pressure, higher temperatures, much lower  $\text{CO}_2$  content and much higher  $\text{NO}_x$  content.

An attempt was made to run the base simulation at conditions as similar as possible to conditions presented by Loutet for the upper absorption section. The base simulation did not converge well at the Loutet conditions, which is not surprising considering completely different

column sizing, flow rates, gas composition, etc. However, the base simulation at the same gas NO<sub>x</sub> concentration, pure water feed and inlet temperatures produced similar results as shown in Figure 7. Inlet and outlet NO<sub>x</sub> concentrations are nearly identical to measured industrial data presented by Loutet. The more rapid initial absorption in the base simulation compared to Loutet is likely due to faster reaction of NO in the gas phase (reaction R1) with high O<sub>2</sub> content and increased solubility of gasses at higher pressure.

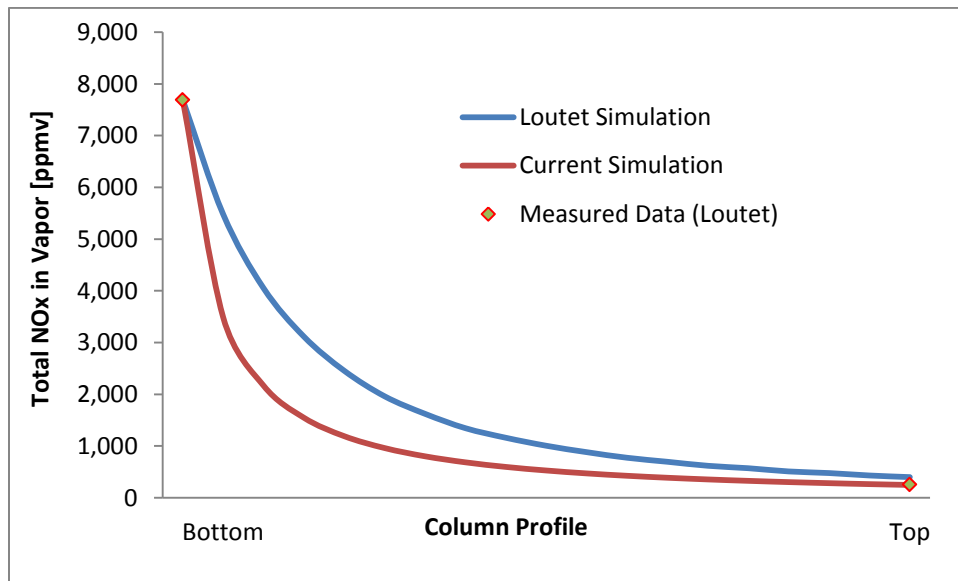


Figure 7 – Base simulation compared to simulation and measured data by Loutet et al.

### 2.12 Sensitivity Analysis

Considerable difference exists in the kinetic parameters presented in the literature. To investigate the sensitivity of the model to these parameters, the kinetic parameters ( $k$  or  $K_{eq}$ ) were varied as shown in Table 7.

Reaction #	-10%	k or K <sub>eq</sub>	+10%
1	1.0800E+03	1.2000E+03	1.3200E+03
2	1.0111E+01	1.1235E+01	1.2358E+01
3	-2.9717E+01	-2.7016E+01	-2.4314E+01
4	2.0923E-12	2.3248E-12	2.5573E-12
5	4.2750E+12	4.7500E+12	5.2250E+12
6	1.5297E+04	1.6997E+04	1.8697E+04
7	1.9800E+13	2.1953E+13	2.4148E+13
8	4.2292E+07	4.6991E+07	5.1690E+07
9	9.9000E+04	1.1000E+05	1.2100E+05
10	1.1139E+04*	1.1700E+04	1.2870E+04
11	2.1722E+22*	2.2394E+22	2.4633E+22
12	1.4688E+09	1.6320E+09	1.7952E+09
13	4.8690E+06	5.4100E+06	5.5723E+06*

\* simulator unstable - adjustment changed to 3% for these parameters

*Table 7 – Kinetic constants and equilibrium coefficients used for sensitivity analysis*

Results of the sensitivity analysis are shown in Table 8. Indicated values are the amount of change of % NO capture vs. the base case simulation. The results clearly show that the most critical parameters are reaction R1, the gas phase reaction of NO<sub>2</sub> with oxygen to produce NO, and the reaction of NO and NO<sub>2</sub> with H<sub>2</sub>O in the gas phase.

Reaction #	-10 %	+10 %
R1	-1.4952	1.2725
R2	0.0001	-0.0001
R3	-5.3132	0.7223
R4	0.0000	0.0000
R5	-0.0001	0.0001
R6	0.0002	-0.0002
R7	0.0000	0.0000
R8	0.0000	0.0000
R9	0.0000	0.0000
R10	0.0000	0.0000
R11	0.0054	-0.0162
R12	0.0000	0.0000
R13	0.0000	0.0000

*Table 8 – Simulation sensitivity to changes in kinetic parameters. Values indicate the change in % NO removal with -10 % and +10 % change in kinetic parameters for each reaction*

### 3 Formation of Aerosols

#### 3.1 Definition of Aerosols

Schaber [24] describes aerosols as “suspensions of particles and gasses which can be considered as stable systems in a gravitational field within a certain space of time”. That is, particles which at least for the short term do not fall by gravity, or that transport through the gas through some other attraction mechanism, qualify as aerosols. Examples are smoke and fog, kept aloft by Brownian motion or air currents. Rain clearly does not qualify. If the particles are solid, the aerosol is referred to as a smoke or fume [25,26]. Fog, which is most important in absorption processes, is more specifically described as a suspension of liquid droplets in gas [27].

In addition, aerosols can be classified by size. The most often cited range for aerosols is 0.01 - 10  $\mu\text{m}$  diameter [25]. Aerosol size depends on the composition and formation mechanism, and can vary widely from process to process as indicated in Table 9 [25,28].

Aerosol	Size ( $\mu\text{m}$ )
Clouds and fog	>2
Hydrochloric acid mist	1 - 3
Sulfuric acid mist	0.3 - 1.5
Ammonium chloride fume	0.05 - 1
Aitken nuclei (atmospheric condensation nuclei)	0.005 - 0.3

Table 9 – Typical particle size of aerosols

#### 3.2 Formation Mechanisms

Aerosol formation only occurs if the gas is supersaturated. Supersaturation is defined as that point in which the volume of condensable components in the gas phase exceeds the equilibrium composition.

Saturation can be quantified by the saturation ratio  $S$  defined as the ratio of the partial pressure of all condensing components to the equilibrium partial pressure [25,31]:



$$S = \frac{\sum p_i(T, y_i)}{\sum p_i^{eq}(T, y_i)} \quad (43)$$

where

$i$  = condensing component

$p_i$  = partial pressure of component  $i$

$p_i^{eq}$  = equilibrium partial pressure of component  $i$

The calculation is limited to only those components that can condense at the stated conditions.

Supersaturation of the gas phase, that is  $S > 1$ , can occur by several different mechanisms [19]:

1. Chemical reactions in the gas phase followed by desublimation of the generated substances. An example is ammonium chloride salts formed in gas containing hydrogen chloride and ammonia. The resulting aerosols can be referred to as reaction aerosols [3].
2. Simultaneous heat and mass transfer that result in a crossing of the dew point line. Resulting aerosols are referred to as condensation aerosols.

Reaction aerosols can generally be avoided by adjusting process parameters such as reactant concentration or pH. For industrial absorption and gas cleaning processes, condensation aerosols are of primary interest.

In the supersaturated environment molecules must initially form molecular clusters before they can begin to form aerosols. This nucleation has two distinct mechanisms:

1. Homogeneous nucleation. Generally, homogeneous nucleation occurs at high partial pressures of the condensing constituents.
2. Heterogeneous nucleation. Occurs where the condensing component forms around pre-existing particles (nuclei). In flue gas streams, this is usually fine ash particles consisting mostly of carbon, which remain after the bulk ash

removal processes. Farther downstream in the cleaning processes, additional solid chemical constituents such as gypsum particles from the desulfurization units may exist.

If particulate is added to a supersaturated system where homogeneous nucleation can or has formed then both homogeneous and heterogeneous aerosols mechanisms can occur in the same process. For example, Shabunya [3] reported on a system with high partial pressures of condensing components where the concentration of aerosol particles exceeded the initial concentration of nuclei entering. In the absorption of acid gasses in flue gas cleaning, only  $\text{SO}_2$  and  $\text{H}_2\text{SO}_4$  absorption are likely to have the high saturation levels necessary for homogeneous nucleation. For other acid gasses, such as  $\text{HNO}_3$ , heterogeneous nucleation will dominate [31].

Fletcher [32] reported that the size of particles can influence the rate of nucleation. Below  $0.01 \mu\text{m}$  size plays a critical role in the nucleation rate. However, above  $0.1 \mu\text{m}$  nucleation rate is essentially independent of size. For treated flue gasses, the bulk of particles range from  $0.35 - 30 \mu\text{m}$  [33]. For ultrafine particles that can be expected to pass through conventional ash removal systems and reach downstream absorption cleaning processes, particle size range is from  $0.03 - 0.1 \mu\text{m}$  [34]. So it is fairly safe to assume that aerosol nucleation process in flue gas is not appreciably affected by particle size.

After the onset of heterogeneous nucleation, particle formation rates decrease rapidly as seen in Figure 8, as the level of supersaturation decreases with particle growth [24].

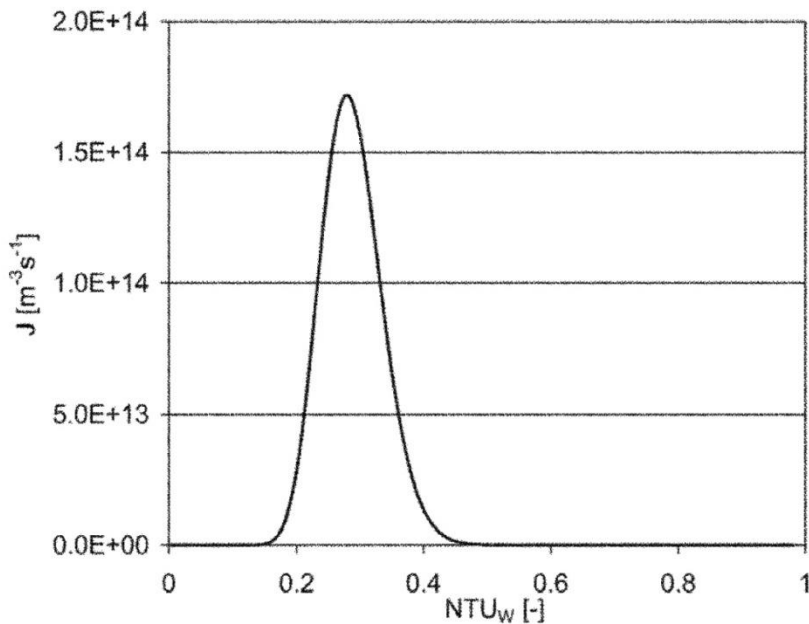


Figure 8 – Humidification of cold air by hot water: nucleation rate ( $J$ ) vs. Number of Transfer Units ( $NTU$ ) according to classical theory [30]

But supersaturation of a gas alone is not sufficient. The saturation ratio  $S$  must also exceed a critical value  $S_{crit}$  [27] where  $S > S_{crit}$ . When  $S$  meets or exceeds  $S_{crit}$  phase transition from gas to liquid can occur using one of the nucleation mechanisms described above. The value of  $S_{crit}$  depends on the nucleation mechanism [27,24].

Homogeneous nucleation occurs at higher saturation ratios  $S = 2 - 5$  [3,25]. Heterogeneous nucleation occurs at much lower saturation ratios  $S_{crit} = 1 - 1.3$  [29,3]. Schaber [35] uses a constant value of  $S_{crit} = 1.02$  for modeling flue gas cleaning processes for all nuclei concentrations ( $C_N$ ) in the typical range of boiler fly ash where  $C_N = 10^4 - 10^6$  particles/cm<sup>3</sup>.

With substances contained in common flue gases and typical scrubbing processes, high saturation ratios are not possible [3] and heterogeneous nucleation is the dominant pathway. In addition, when aerosols grow, nucleation and aerosol growth continues until  $S$  drops below  $S_{crit}$ . At this point, the nucleation process stops and the concentration of particles per volume of gas  $C_N$  remains constant [3]. In flue gasses, the introduction of particles in the early stages of absorption rapidly decreases the saturation levels, reducing the future chance of additional homogeneous nucleation [27] as shown in Figure 9.

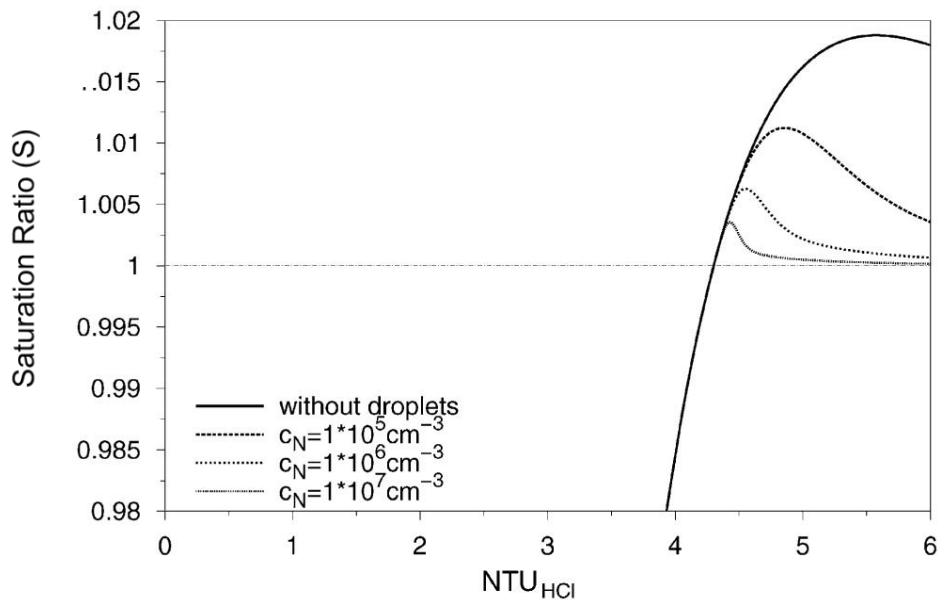


Figure 9 – Calculated saturation profiles for different number concentration of nucleation kernels clearly showing the decrease in saturation with the rapid onset of heterogeneous nucleation.  $NTU_{HCL}$  is the number of transfer units in the modeled HCL absorber, representing increasing transfer area i.e. further down the gas path in the absorption column [31].

### 3.3 Particle Growth

Once initial nucleation takes place, particles continue to grow by condensation of condensable species in the gas phase and by collisions with other particles. If the total concentration of particles is sufficiently small, collision growth is rare and can be safely ignored [24,27].

In flue gas absorption water vapor is the major condensable constituent in the vapor phase, so particle growth is predominately due to the condensation of water vapor. The water droplets can be assumed to be in equilibrium with the surrounding gas phase.

In the gas phase, fine aerosol particles follow the gas path at the same velocity as the bulk gas. Absorption or deposition of the aerosol particles back into the liquid phase can be ignored as typical absorbers have little effect on extremely light particles [24].

After the onset of heterogeneous nucleation, particle formation rates decrease rapidly as seen in Figure 8 as the level of supersaturation decreases with particle growth. For packed columns, particle formation can occur in the first 3 – 10 seconds [24]. The composition of the particles may continue to change as the established particles reach equilibrium with the surrounding gas stream.

The higher the concentration of droplets the smaller the diameter of the droplets as shown in Figure 10. This arises from the fact that droplet size can increase only until saturation  $S = 1$  is reached. A finite amount of vapor is available between  $S_{crit}$  and  $S=1$ .

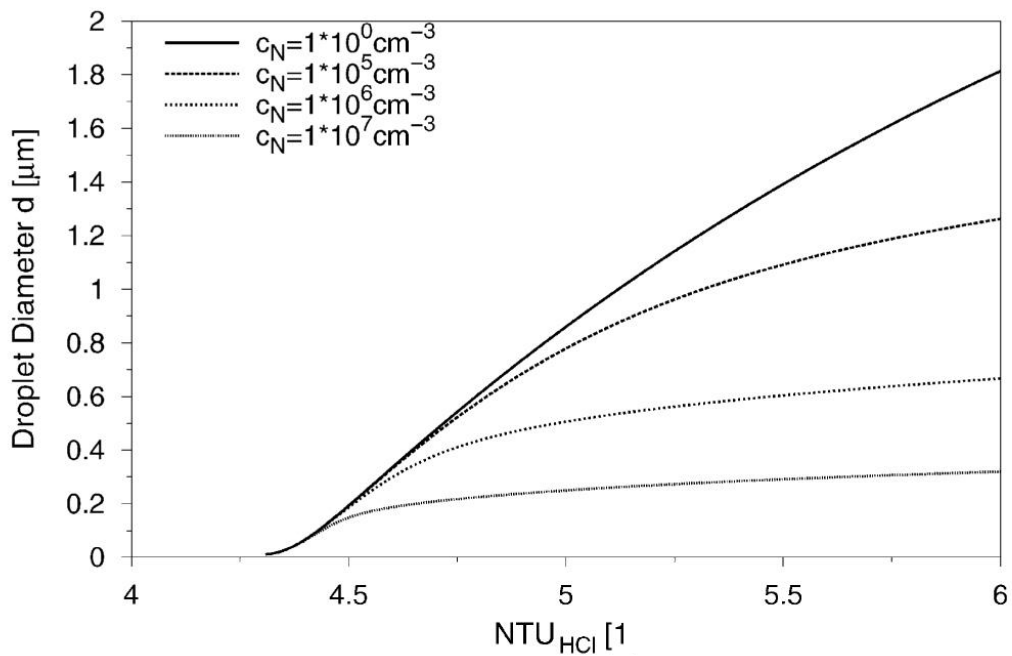


Figure 10 – Calculated droplet diameter in the quench for different concentrations of nucleation kernels [31]

### 3.4 Characterization of Particulate Nuclei

With nuclei concentration playing such an important part in the formation of aerosols in absorption processes, quantifying the concentration of particulate entering the process is essential to predicting aerosols and their effect on absorption.

Much research has been done on boiler particulate because of its effect on atmospheric aerosol formation. A typical electrical generation coal fired boiler configuration is shown in Figure 11. Ash from boilers typically has a bimodal size distribution as shown in Figure 12, with the bulk of the mass in the  $> 1 \mu\text{m}$  diameter size range.

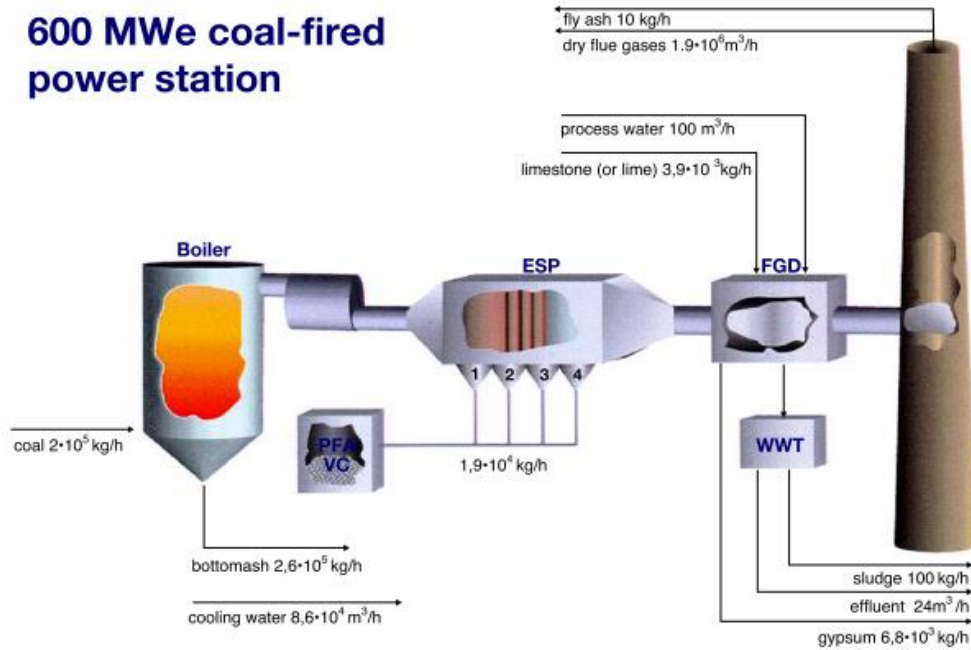


Figure 11 – A typical coal fired power station [36]

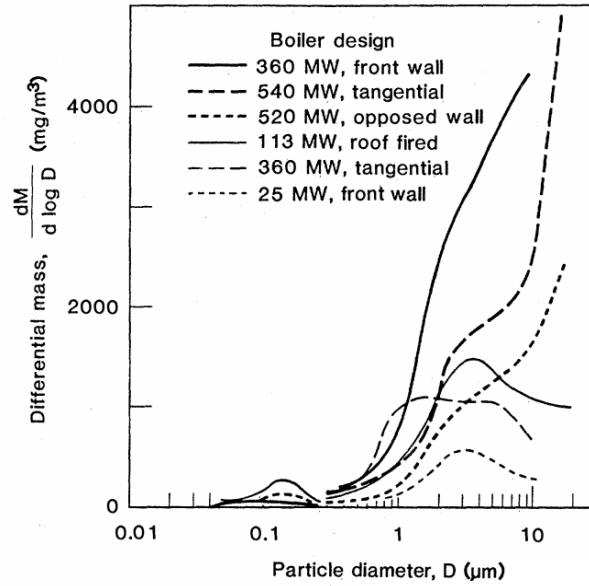


Figure 12– Summary of differential size distribution at the outlets of six coal fired utility boilers of various capacities and firing methods [37]

After the boiler, the flue gas enters some type of bulk ash removal system, most often an ESP (Electrostatic Precipitator) or filter baghouse. Gladney [34] reports that 96% of the boiler ash is removed in the bulk ash removal processes. These processes are most efficient at removing the larger and heavier particles while many of the sub-micron diameter particles pass through [38]. The result is a substantially reduced ash load more heavily distributed to particles  $< 5 \mu\text{m}$  diameter size as shown in Figure 13. But most ultrafine particles pass through the bulk removal processes [38]. For the purpose of this investigation, 10% removal of ultrafine particles is assumed for the bulk removal processes.

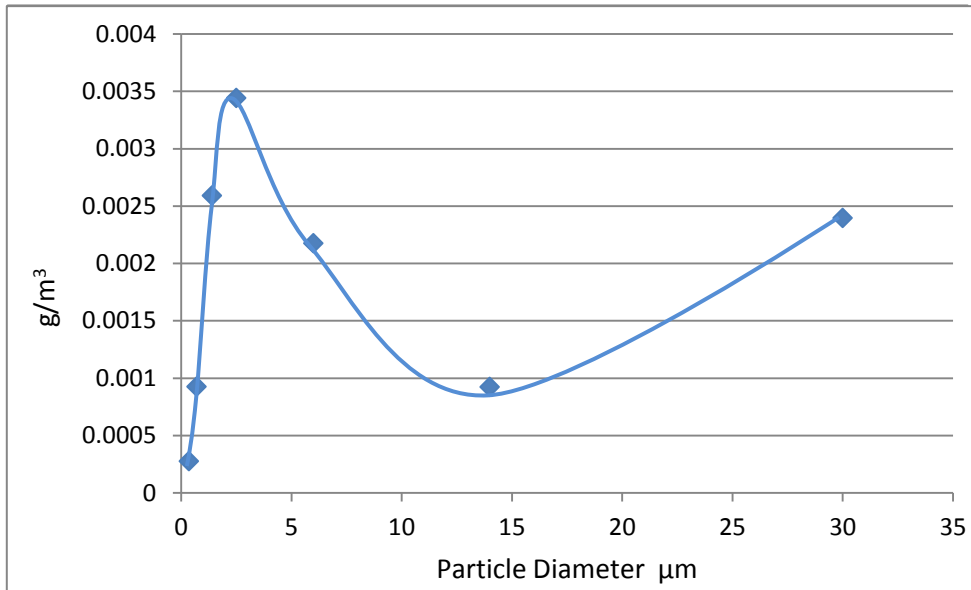


Figure 13 – Particle size distribution after ESP (electrostatic precipitator). Based on data from Gladney [34].

After bulk ash removal nearly all modern electrical generation boilers have additional scrubbing for the reduction of SO<sub>2</sub> gas. These are most often aqueous absorption systems, the most common being Wet Flue Gas Desulfurization (WFGD) systems using alkaline slurries or ammonia solutions in a spray tower. WFGD removes a significant amount of particulate, reported by Meij [36] and Wang [39] at 80% and 74.6%, respectively. Like the bulk ash systems, WFGD also tend to be more efficient at removing larger particles. In addition, fine particles of sorbent may be added to the flue gas stream as a result of the absorption process as shown in Table 10. Yan [40] reported that in ammonia based FGD processes, total emitted particulate may actually increase out of the WFGD.

Source	Fly ash	Limestone	Gypsum
Meij [36]	40	50	10
Wang [39]	45	47.5	7.9

Table 10 – Composition of particulate (%w) after WFGD



With few oxy-fired boilers in commercial operation, less data is available to determine typical particle compositions out of the boiler and into subsequent gas cleaning operations. Morris [33] compared the production of soot and unburned carbon ash particles in conventional and oxy-fired coal boilers. Results (Figure 14) show approximately 70% reduction in fly ash produced by oxy-fired boiler (~2.5% O<sub>2</sub> concentration in flue gas) compared with conventional boilers (~1% O<sub>2</sub> in flue gas).

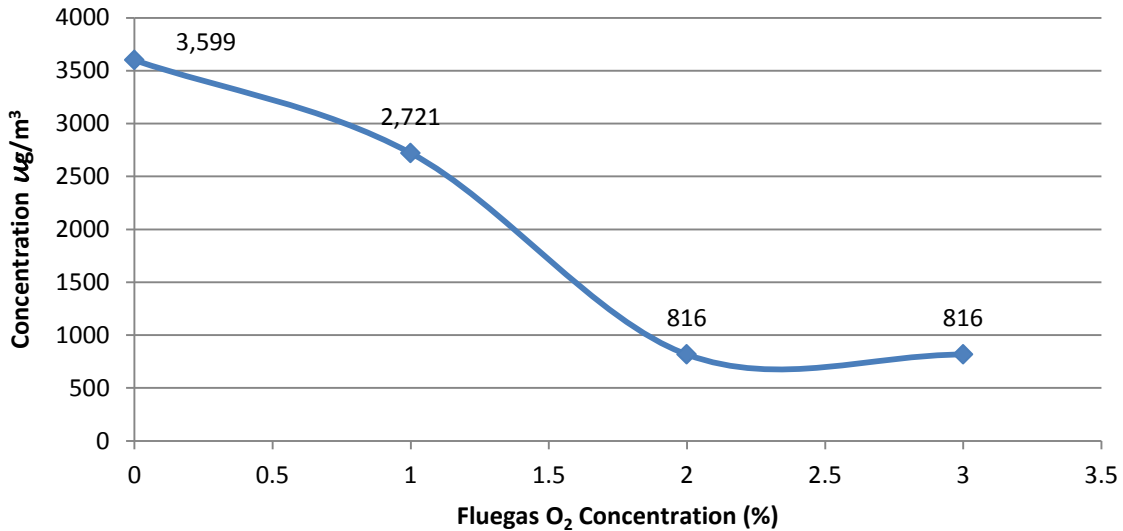


Figure 14 – Ultrafine (0.1 – 1 μm) particulate concentration in flue gas vs. flue gas O<sub>2</sub> concentration on Utah coal. Data extracted from Morris [33]

To estimate aerosol formation from heterogeneous nucleation, the concentration of nuclei must be known. The optimum source of information for accurate prediction of aerosols in a live industrial process is actual measurement of particles feeding the absorption unit. However, these measurements can be difficult and costly to obtain. In live processes, the measurements can be complicated by moisture content and formed aerosols already present in the gas stream.

For the purpose of this investigation to estimate potential existence and effects of aerosols on GPU (gas processing unit) absorption, an estimate on nuclei size and concentration was needed based on available data. The method below summarizes the straight forward calculation method. This process can be modified with actual process data when it is available.

Required data is particle size, particle concentration, removal efficiency of any intermediate processes and density of the particulate. Table 11 list data used and Table 12 lists the resulting particle concentrations used after straightforward calculations.

Source	Property	Value	Units
Moris [33]	Oxy boiler exit particulate concentration	0.000816	$g/cm^3$
Gladney [34]	Ash removal in bulk ash system	96	% removal
Wang [39]	Ash removal in WFGD	74,5	% removal
Andriano [38]	Ash density	2.7	$g/cm^3$
Meij [36]	Remaining fine ash particle size	0.55	$\mu m$ diameter

Table 11 – Data used for calculation of nuclei to GPU NO<sub>x</sub> absorption process

Property	Value	Units
Particle mass exiting WFGD	$4.0 \times 10^{-6}$	$g/cm^3$
Volume of individual particle (assuming spherical shape)	$8.7 \times 10^{-20}$	$m^3$
Particle concentration entering GPU	$1.7 \times 10^7$	$particles/m^3$
Particle concentration entering NO <sub>x</sub> absorption process	$4.34 \times 10^6$	$particles/m^3$

Table 12 – Calculated particle properties. Particle concentration entering GPU is estimated as the low end concentration expected with removal by bulk removal processes and WFGD. Particle concentration entering NO<sub>x</sub> absorption process assumes an additional stage of particulate removal through a GPU lead chamber absorber with the same particulate removal efficiency as a WFGD. This is considered the low end of the concentration range expected.

The particulate entering the GPU could be expected to form aerosols in the initial SO<sub>2</sub> absorption stage if sufficiently saturated conditions are present. However, if aerosol formation does not take place, the particulate would be expected to pass through the initial absorber unscathed with the gas flow to the following process.

Two potential scenarios can then be considered for estimation of the effect of aerosols:

1. Aerosols formed in a previous absorption process reach the NO<sub>x</sub> process in aerosol form. These particles would reach equilibrium with the NO<sub>x</sub> process gas.
2. Particulate directly from the boiler ash cleaning processes reaches the NO<sub>x</sub> absorber in particulate form. This particulate would then be nuclei for formation of aerosols provided favorable conditions exist. This may be representative of both GPU SO<sub>2</sub> and NO<sub>x</sub> absorption processes and may also apply to other wet absorption processes such as amine or ammonia CO<sub>2</sub> removal.

### 3.5 Modeling and Prediction

#### 3.5.1 Saturation Ratio

The most important parameter to determine the potential for aerosol formation is the saturation ratio  $S$  defined in equation 43, because nucleation cannot occur unless  $S > S_{crit}$ .

In Aspen, the RadFrac block can be run in either equilibrium or rate-based mode. The NO<sub>x</sub> reactions are exothermic. In an actual process, the absorption column is not likely to be sized so generously that it is in full equilibrium condition. More likely, the gas liquid interface could be considered in equilibrium, while the bulk gas phase would be expected to be in some transitional state between the current stage and the previous stage. In order to simulate the thermal gradient between the gas and liquid throughout the column the RadFrac block must be in rate-based mode.

An initial calculation of  $S$  for water vapor on each stage  $n$  was completed using Aspen data per Equation 44:

$$S = \frac{\text{Partial pressure of gas phase water}}{\text{Equilibrium partial pressure of water at } T_{g_n}} \quad (44)$$

It is important that the proper temperatures be taken from the Aspen model for use in the calculation. In Figure 15 below, the gas flowing to stage  $n$  is at gas temperature  $T_{g_{n+1}}$  and partial pressure composition of  $p_{g_{n+1}}$ . This gas is contacting liquid at temperature  $T_{l_n}$ . The interface

temperature rapidly reaches the temperature of the bulk liquid phase. Aspen predicts the bulk liquid temperature as being virtually indistinguishable from the interface temperature in this model.

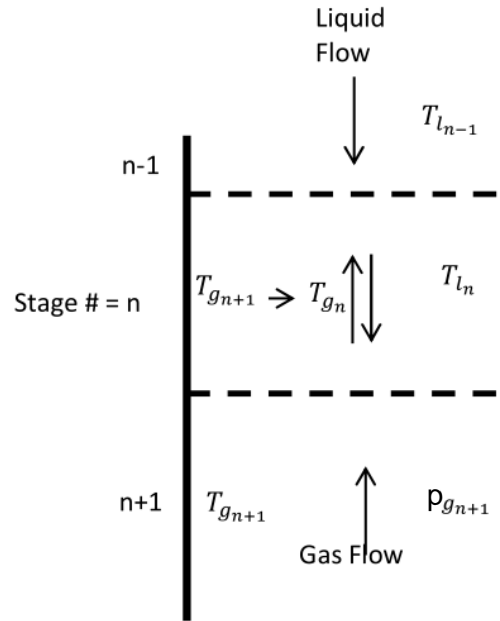


Figure 15 – Gas and liquid temperature interactions in one stage of packed absorber column

If you assume that heat transfer at the interface takes place faster than the reactions and mass transfer in the bulk gas, then it is reasonable to assume that stage n is near the concentration of the previous gas stage, so the gas experiences first a change in temperature to the interface temperature, but at the higher concentration of the previous stage, i.e.

$$T_{g_{n+1}} \xrightarrow{p_{g_{n+1}}} T_{g_n}$$

So equation 43 can be rearranged using Aspen data to:

$$S = \frac{\sum p_{i_{n+1}}(T_{n+1}, y_{i_{n+1}})}{\sum p_{i_n}^{eq}(T_n, y_{i_n})} \quad (45)$$

A comparison of the two calculation methods is shown in Figure 16. While the difference is small in the base simulation case, the difference can be significant under other conditions where the temperature gradient between vapor and liquid entering a stage is greater.

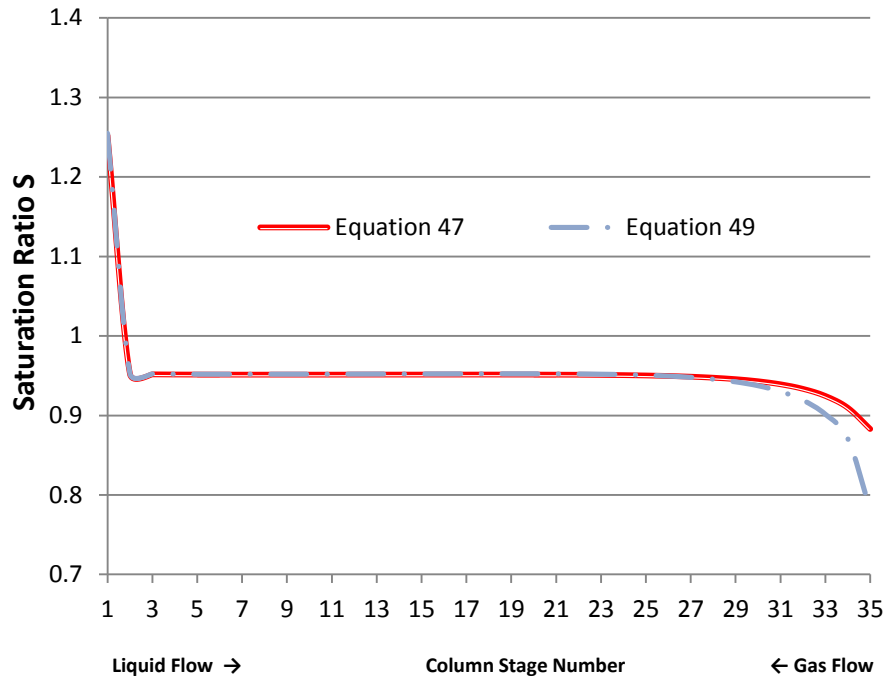


Figure 16 – Comparison of different equation methods to model saturation ratios.

### 3.5.2 Particle Size

Growth by condensation is the predominant mechanism of particle enlargement after nucleation and is strongly influenced by the number of nuclei in the gas [24]. To calculate the growth of droplets, Körber and Schaber [27] used a two-step process:

1. Describe time dependent changes in radius, concentration and temperature using volume, mass and energy balance on a single droplet
2. Solve transport equations in the vapor phase for heat and mass to the droplet.

The process is computationally intensive and not easily applicable in a process environment. However, simulations performed by Ehrlig [31] and Schaber [42] show a general trend of particle size vs. nuclei concentration under various process conditions. It is assumed that the particles reach their maximum steady-state size under saturated conditions. Under actual process conditions, the time or saturation ratio may not be adequate to achieve this size, so this represents the worst case scenario. Using this data plotted in Figure 17, particle size can be estimated using the equation:

$$\text{Droplet diameter } d \text{ (}\mu\text{m)} = -0.3099 \ln(C_n) + 6.1226 \quad (46)$$

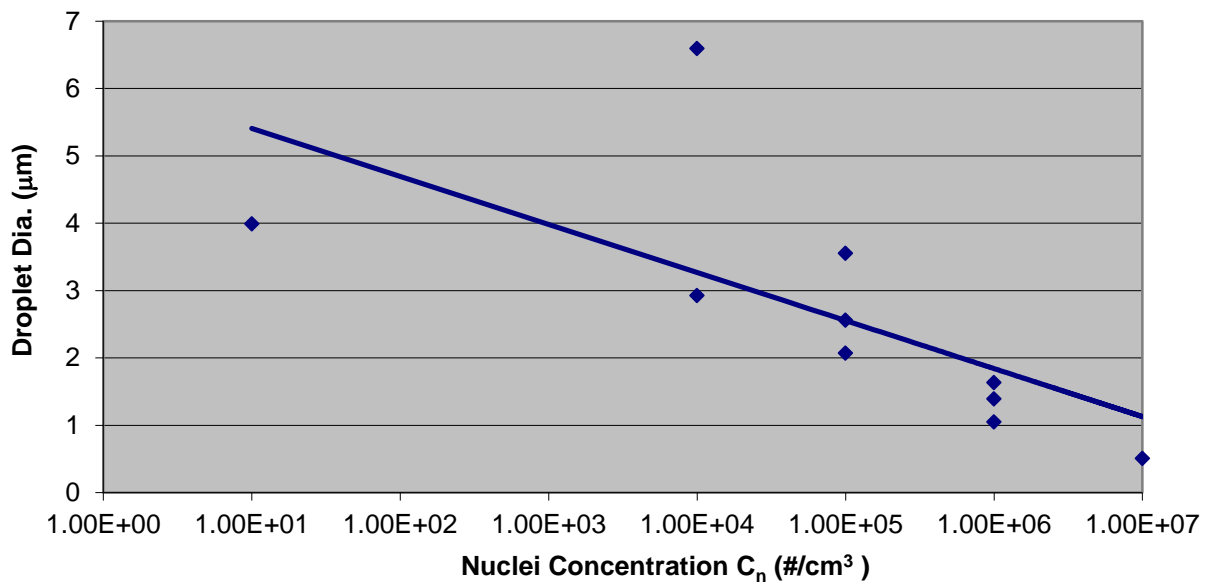


Figure 17 – Maximum particle size vs. nuclei concentration from data extracted from Ehrlig and Schaber [31,42]

## 4 Simulating Aerosol Effects on NO<sub>x</sub> Absorption

Figure 18 shows the overall simplified method used to estimate aerosol effects:

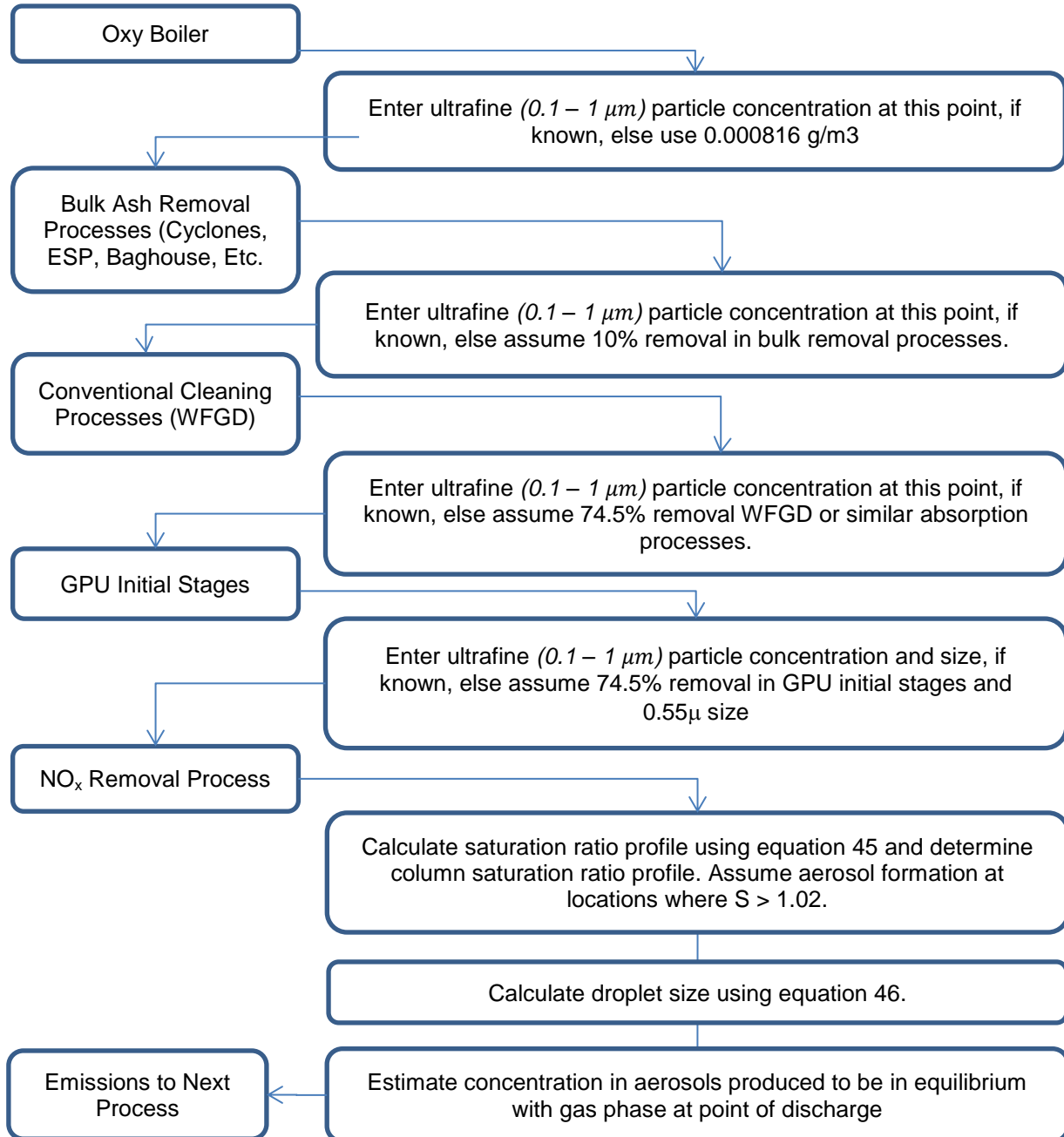


Figure 18 – Flowsheet of calculation process for aerosols effect

## **4.1 Effect of Absorption Variables on Saturation Ratio and NO<sub>x</sub> Removal**

To this point, the saturation ratio  $S$  was determined only for the base absorption case. To determine the potential range of saturation conditions for the modeled absorber, an analysis was performed to test the effect of varying gas and liquid inlet temperature and flow rates on saturation ratio.

Saturation ratios were determined for each case using equation 45.

### **4.1.1 Inlet Gas Temperature**

Inlet gas temperature was varied from 7 to 19 °C at constant liquid inlet temperature of 13 °C and constant gas and liquid flow of 292,107 kg/hr (1.0 L/G). Results are shown in Figure 19 – 22.

NO<sub>x</sub> removal was little affected by inlet gas temperature (Figure 19). Column temperature is highly dependent on the bulk liquid temperature and only affected by gas temperature in the lower stages near the gas inlet as shown in Figure 20 and 21. With Henry's constants dependent on liquid temperature, absorption of NO<sub>x</sub> would not be significantly affected by the gas phase, although the gas phase reaction rate would.

Saturation Ratio (Figure 22) remains well below  $S_{crit} = 1.02$  for the entire column except stage 1 where the hot gas contacts the colder liquid inlet flow.



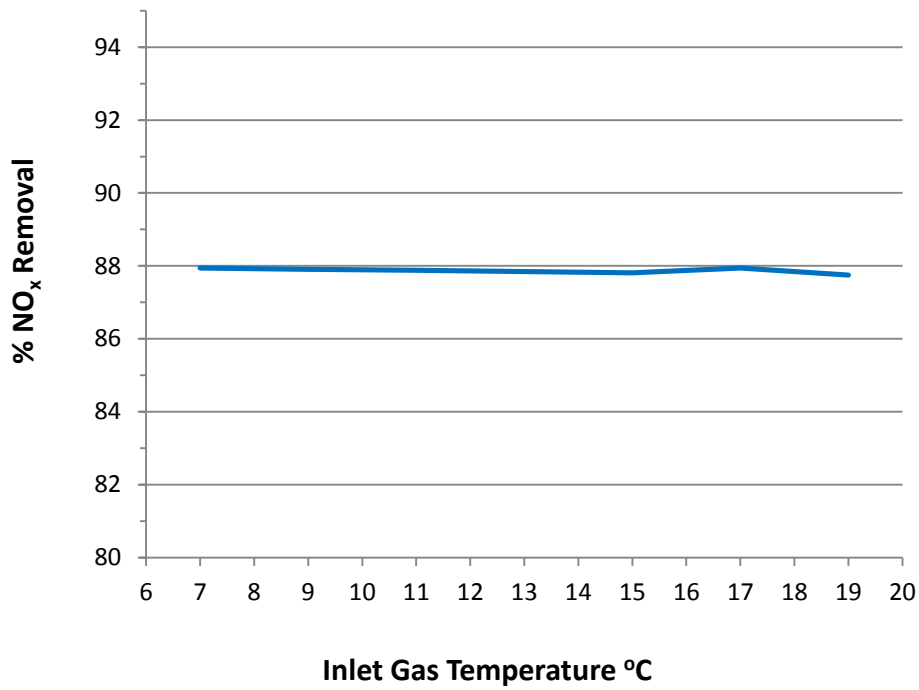


Figure 19 - NO<sub>x</sub> % removal vs. inlet gas temperature

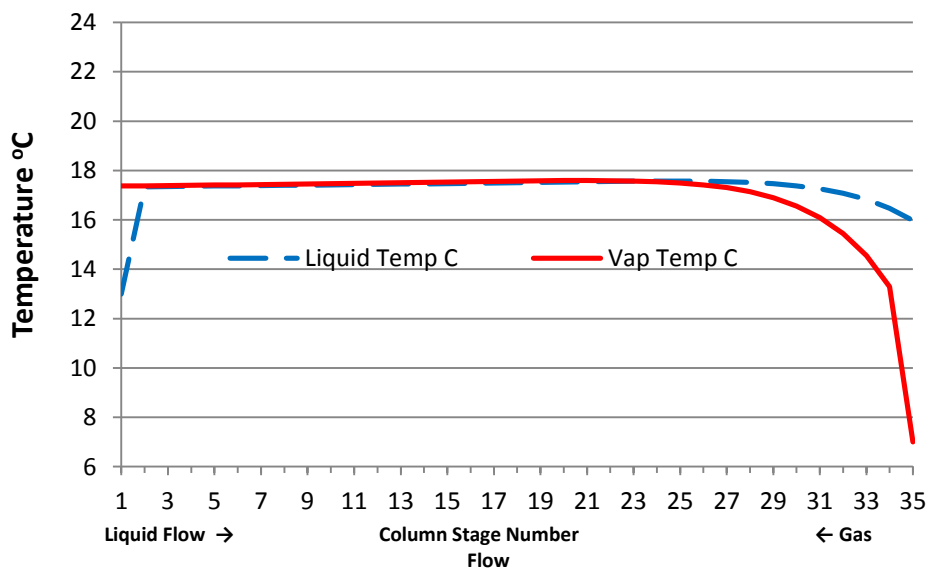


Figure 20 - Column temperature profile – 7°C gas inlet temperature

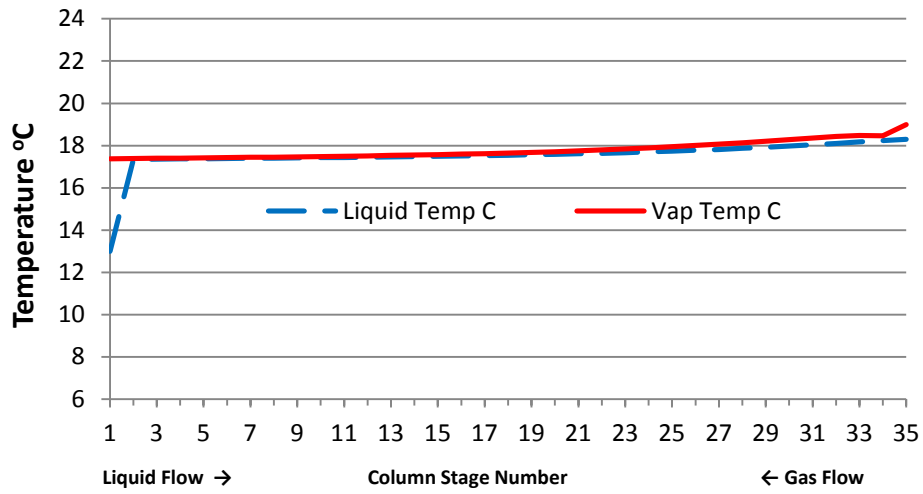


Figure 21 - Column temperature profile – 19°C gas inlet temperature

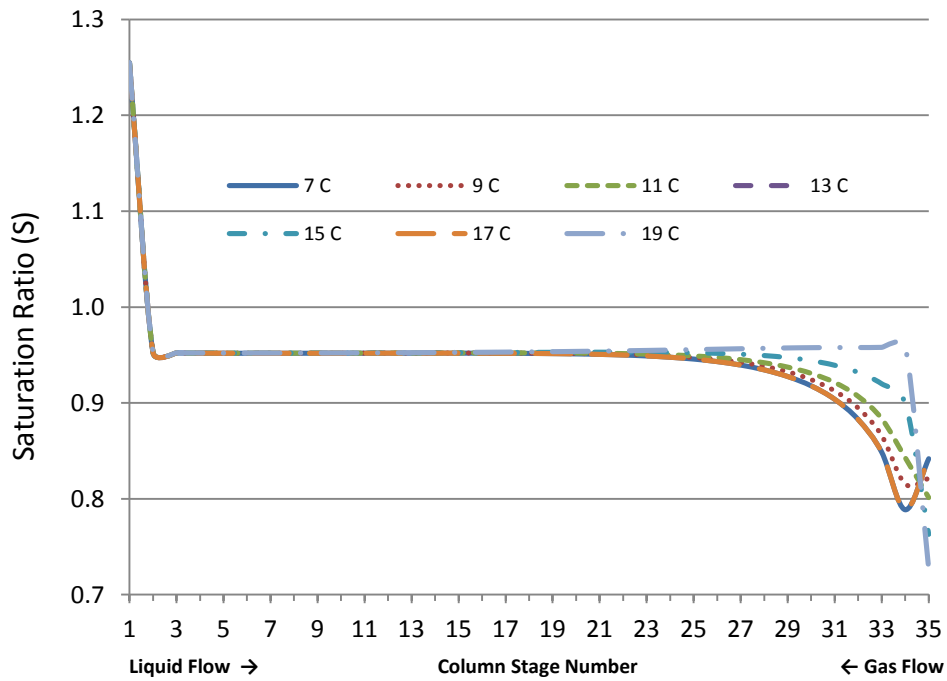


Figure 22 – Effect of inlet gas temperature on saturation ratio

### 4.1.2 Inlet Liquid Temperature

Varying liquid inlet temperature had a significant effect on column temperature profile, absorption rate and saturation ratio. Liquid temperature was varied from 5 to 19 °C at constant gas inlet temperature of 13 °C and constant gas and liquid flow of 292,107 kg/hr (1.0 L/G). Results are shown in Figures 23 - 26.

NO<sub>x</sub> removal increases with decreasing gas temperature as seen in Figure 23 as a result of better absorption of NO<sub>x</sub> components at lower temperatures and an increase in rate of reaction 1. It is worth noting the significant change in column temperature between the low temperature and high temperature case shown in Figures 24 - 25.

Figure 26 shows the effect on saturation ratio. As liquid temperature decreases, the saturation ratio at the gas inlet increases as the colder liquid contacts the hot column gas. However, the increase in saturation ratio at the top of the column from a maximum of  $S = 1.16$  in the high temperature case to  $S = 1.30$  for low temperature is not really that important, since any saturation ratio over  $S_{crit}$  will produce significant and almost instantaneous aerosol.

Of more interest is the increase in saturation ratio at the bottom gas inlet of the column as inlet liquid temperature decreases. At liquid temperatures of 5 and 7 °C, the gas inlet stages also exceeds  $S_{crit}$ . This means that aerosols will form at the bottom of the column and proceed upwards through the entire column, likely reaching equilibrium saturation with the NO<sub>x</sub> pollutants during their journey.

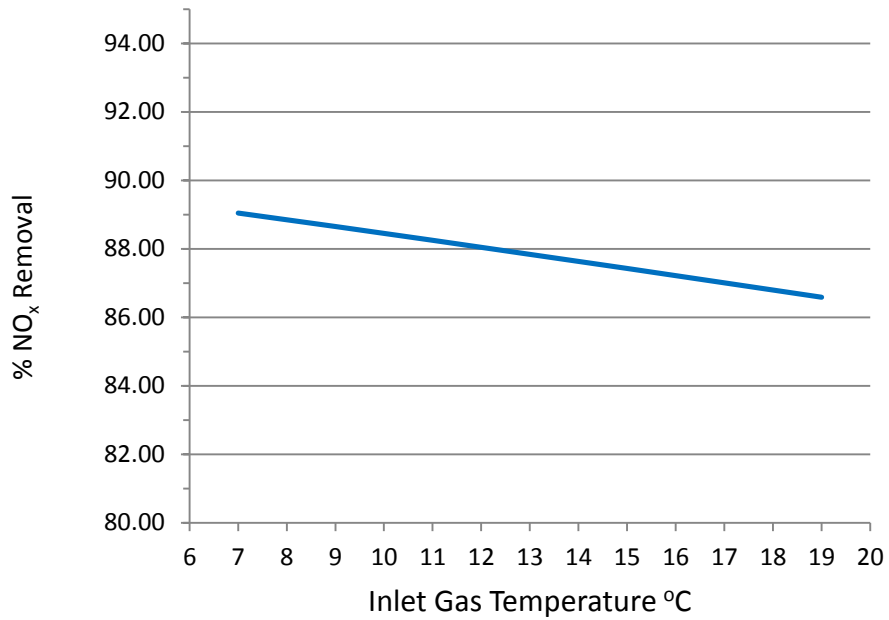


Figure 23 - NO<sub>x</sub> % removal vs. inlet gas temperature

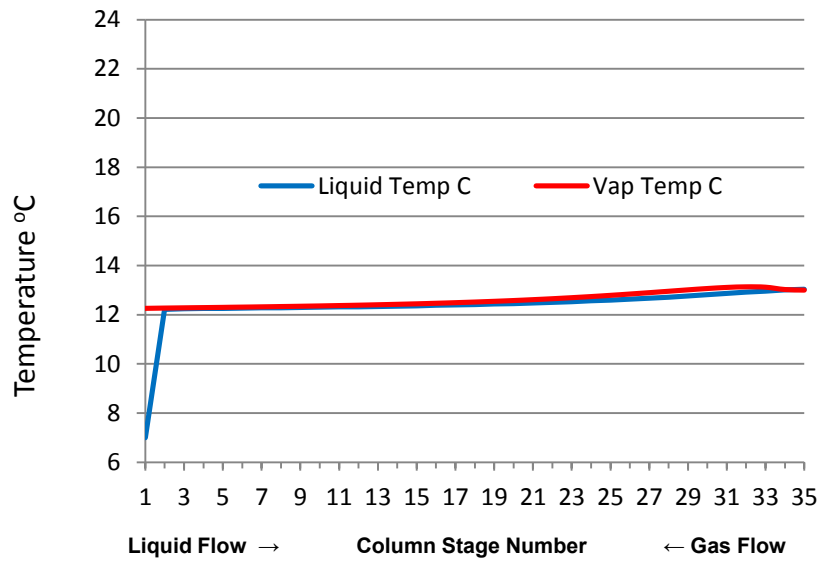


Figure 24 - Column temperature profile – 7°C liquid inlet temperature

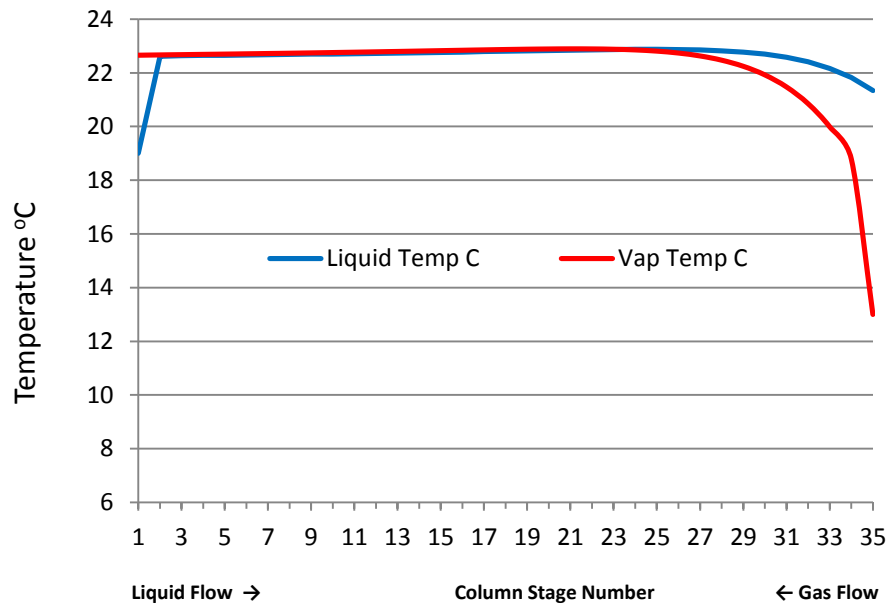


Figure 25 - Column temperature profile – 19°C liquid inlet temperature

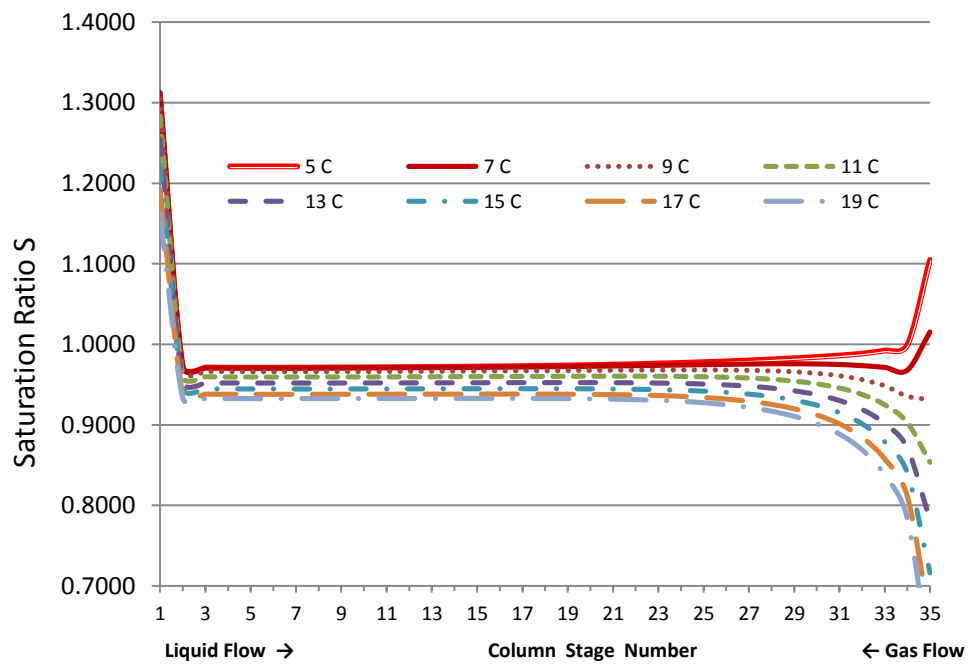


Figure 26 – Effect of liquid inlet temperature on saturation ratio

### 4.1.3 Inlet Gas Flow

Inlet gas flow was varied  $\pm 20\%$  over the base flow of 292,107 kg/hr. Not surprisingly,  $\text{NO}_x$  removal increases at lower gas flow since both the rate based conversion of  $\text{NO}$  to  $\text{NO}_2$  and absorption will increase with increased column residence time. Column temperature profile was virtually unchanged by gas flow rates. Saturation ratio is likewise unchanged as shown in Figure 29.

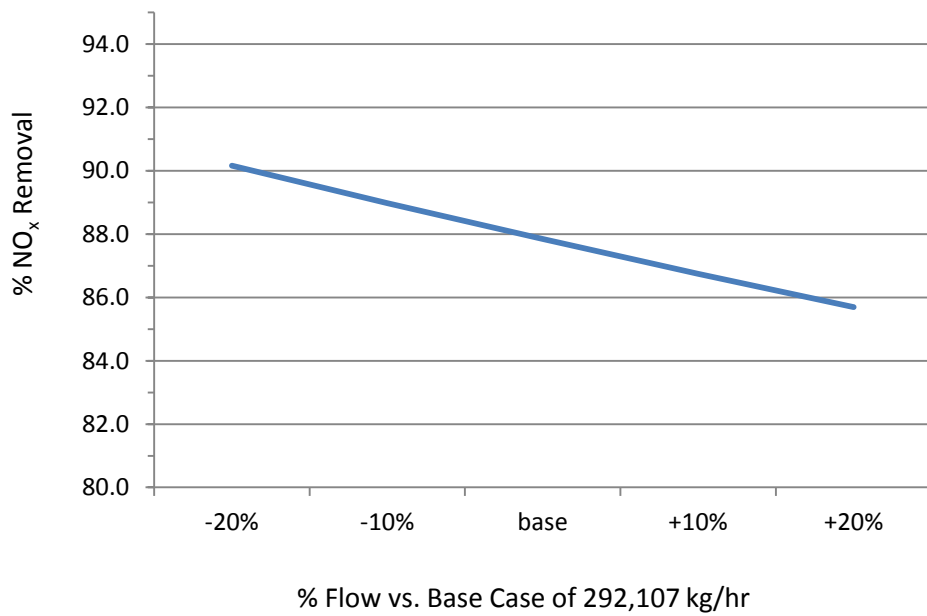


Figure 27 -  $\text{NO}_x$  % removal vs. inlet gas flow

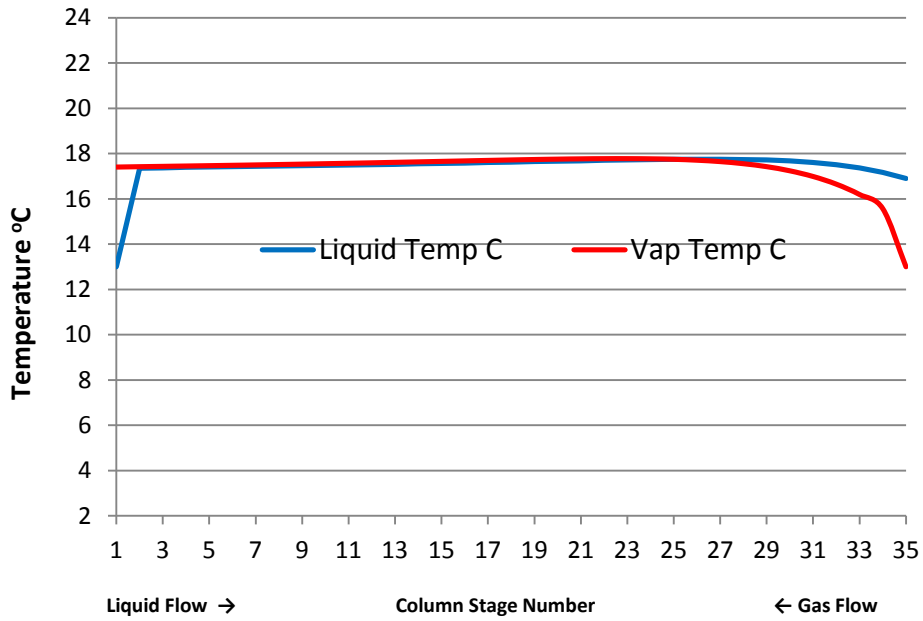


Figure 28a - Column temperature profile comparison at +20% gas flow

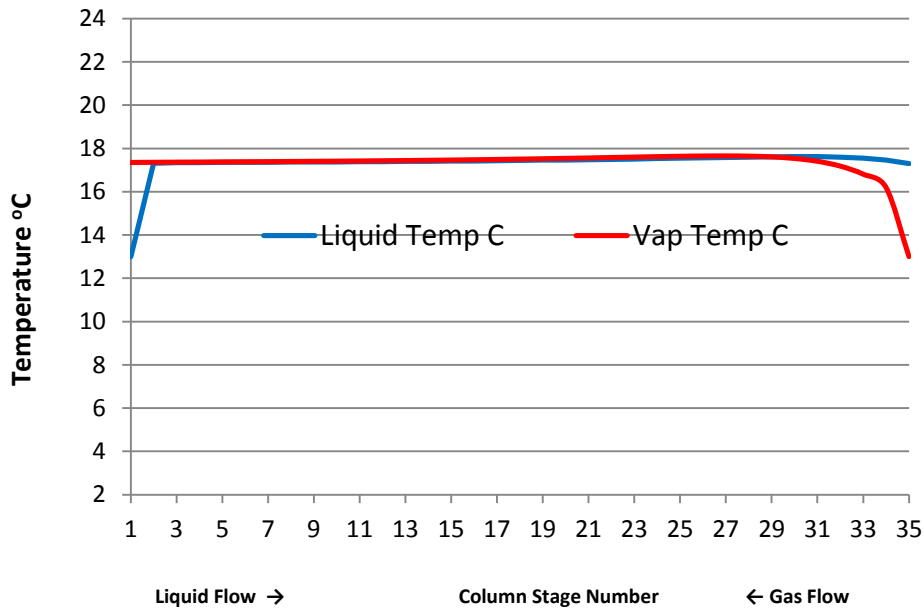


Figure 28b - Column temperature profile comparison at -20% gas flow

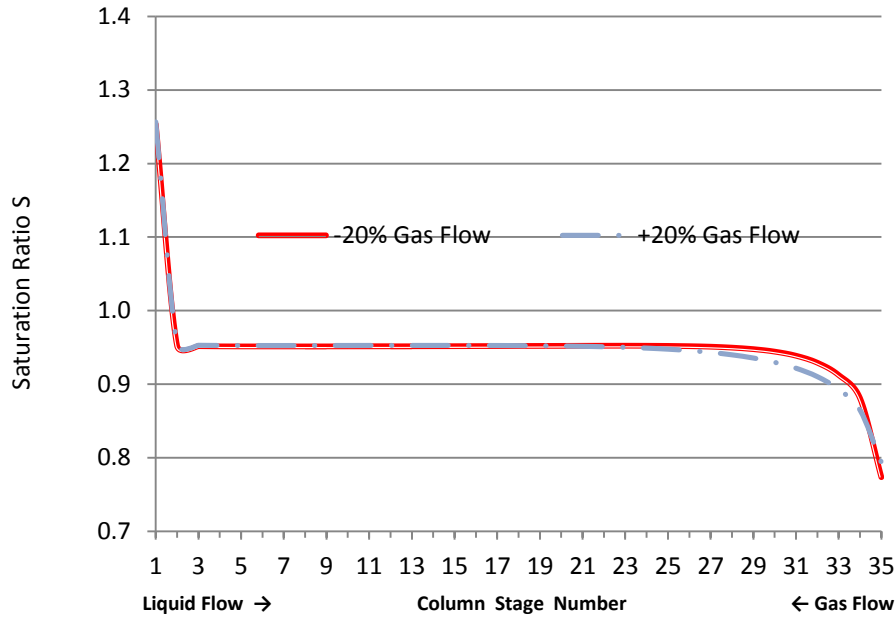


Figure 29 – Effect of gas flow rate on saturation ratio

#### 4.1.4 Inlet Liquid Flow

Inlet gas flow was varied -20% to +15% over the base flow of 292,107 kg/hr. The simulation was not stable at liquid flows over +15%, probably due to flooding conditions of the packing. Similar to changes in gas flow, changes in liquid flow resulted in marginal changes in NO<sub>x</sub> removal rate, and had little effect on column temperature profile or saturation ratio.



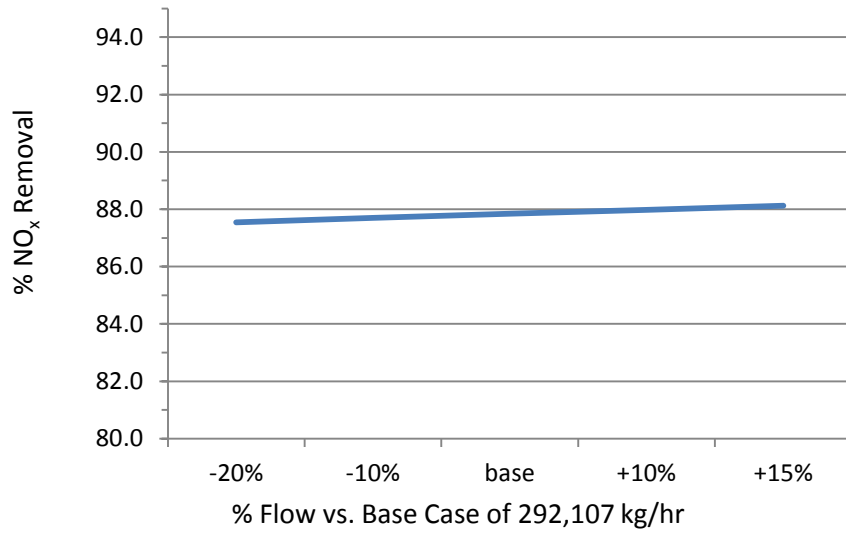


Figure 30 - NO<sub>x</sub> % removal vs. inlet liquid flow

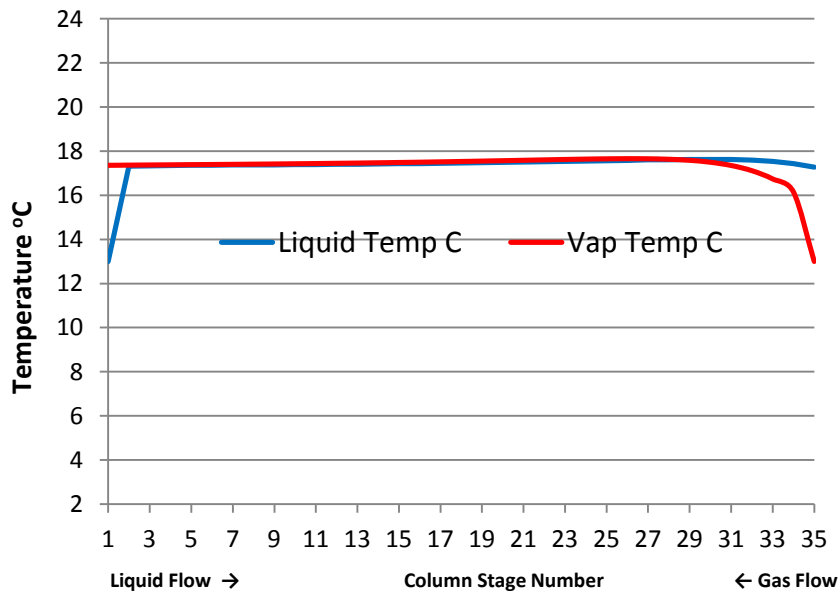


Figure 31a - Column temperature profile comparison at +15% liquid flow

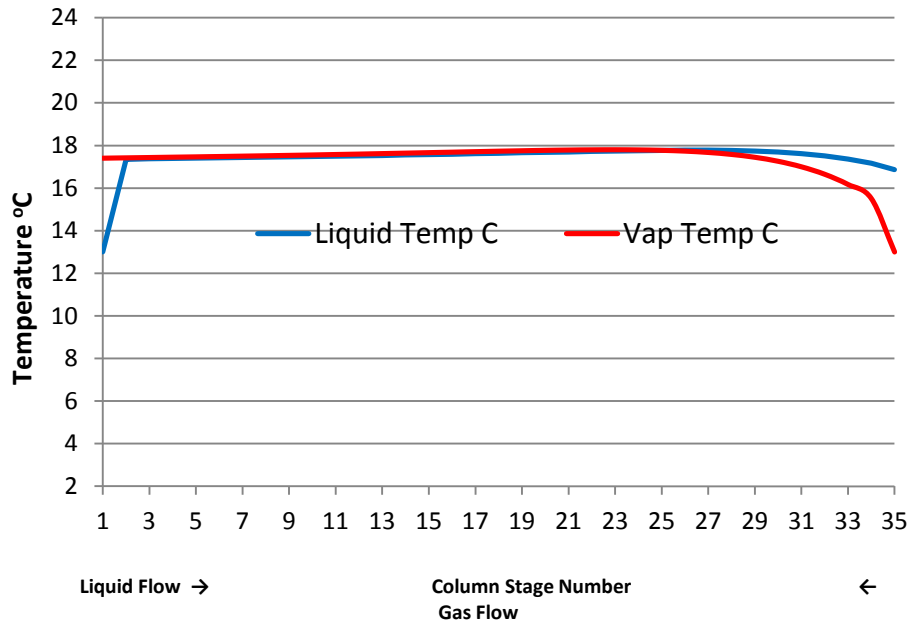


Figure 31b - Column temperature profile comparison at -20% liquid flow

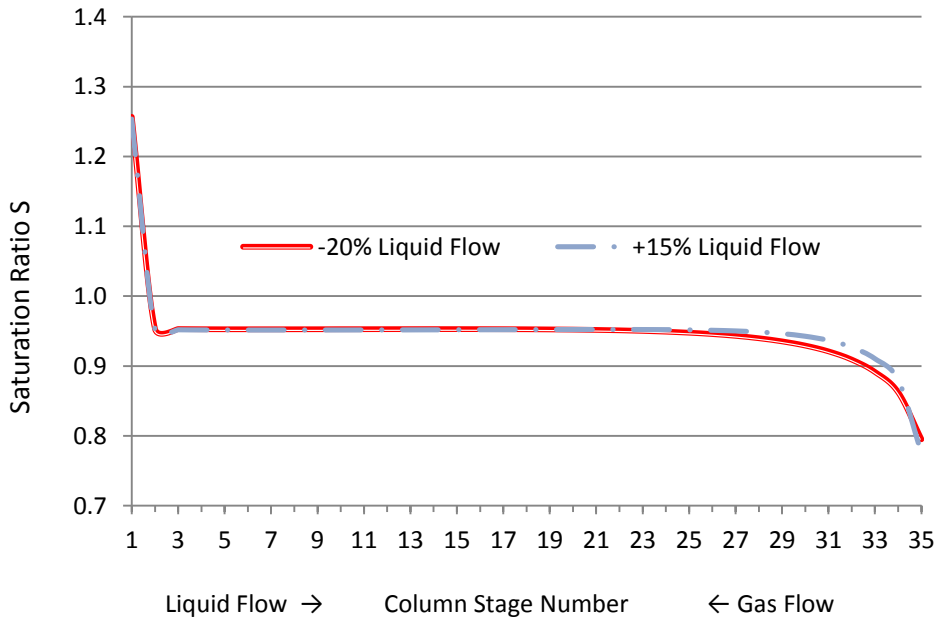


Figure 32 – Effect of liquid flow rate on saturation ratio

#### 4.1.5 Liquid/Gas Temperature

Various combinations of liquid and gas temperature were tested to determine the range of saturation conditions that could be simulated. The following temperature combinations were tested:

Inlet Gas/Liquid Temperature (°C)
21 / 3
19 / 5
17 / 7
15 / 9
13 / 11
11 / 13
9 / 15
7 / 17
5 / 19

*Table 13 – Simulated liquid / gas inlet temperature combinations*

Percent NO<sub>x</sub> removal varied significantly over this range, with lower liquid temperature clearly favoring improved removal as shown in Figure 33.

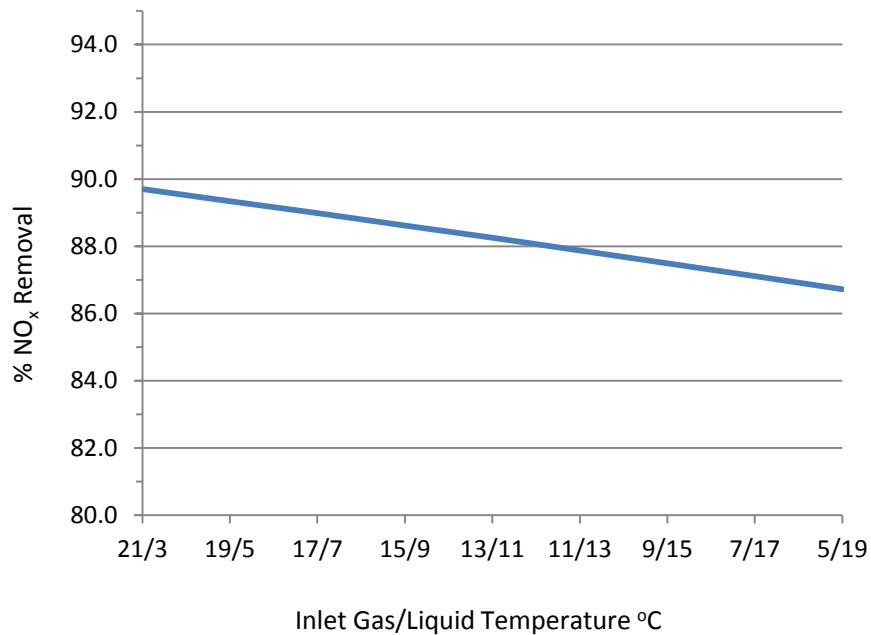


Figure 33 - % NO<sub>x</sub> removal vs. various inlet gas and liquid temperature

Column temperature profiles were significantly different at the extremes as shown in Figure 34 – 35. But the most significant result was the effect on saturation ratio. At high gas and low liquid temperatures, saturation ratio was above  $S_{crit}$  in the bottom seven stages of the absorber. In the presence of heterogeneous nuclei, fully developed aerosols would form at the early stages in the column.

Although not modeled in this study, a similar effect would be expected if the absorber column had intermediate cooling of the liquid flow as is common for absorbers of this type.

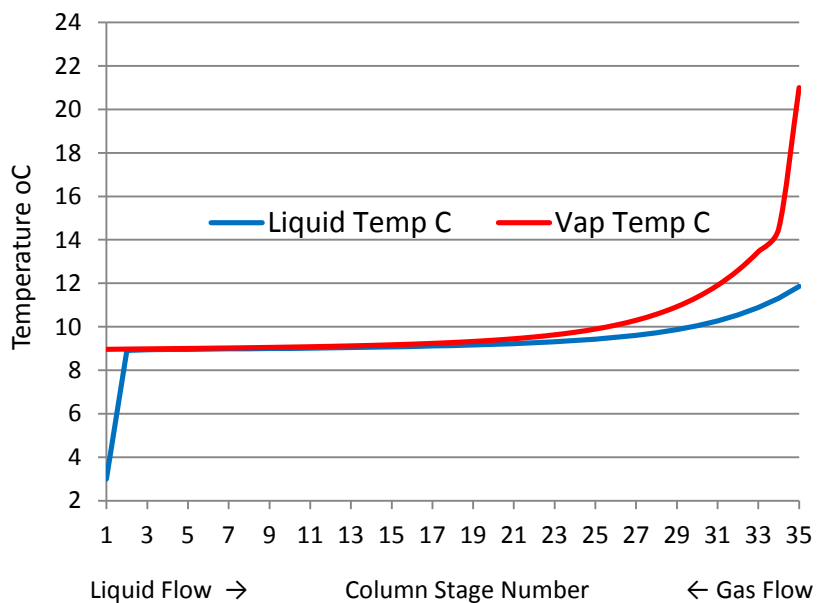


Figure 34 - Column temperature profile at 21/3 °C gas/liquid inlet temperature

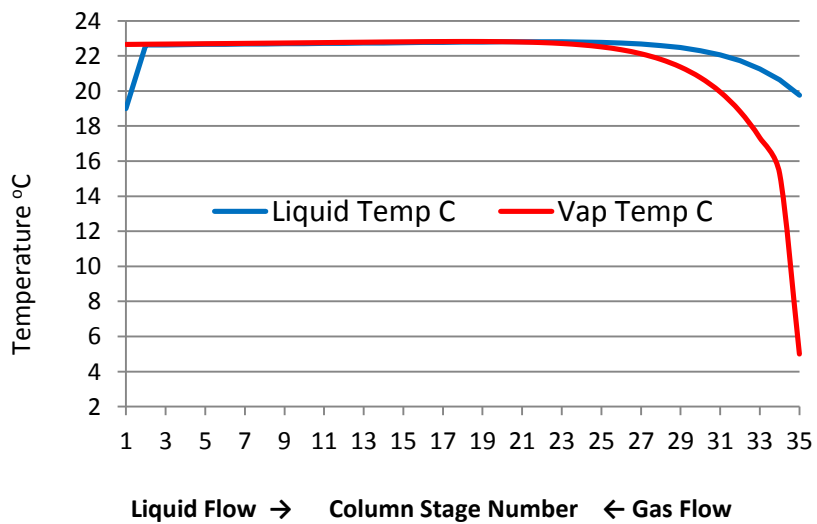


Figure 35 - Column temperature profile at 5/19 °C gas/liquid Inlet temperature

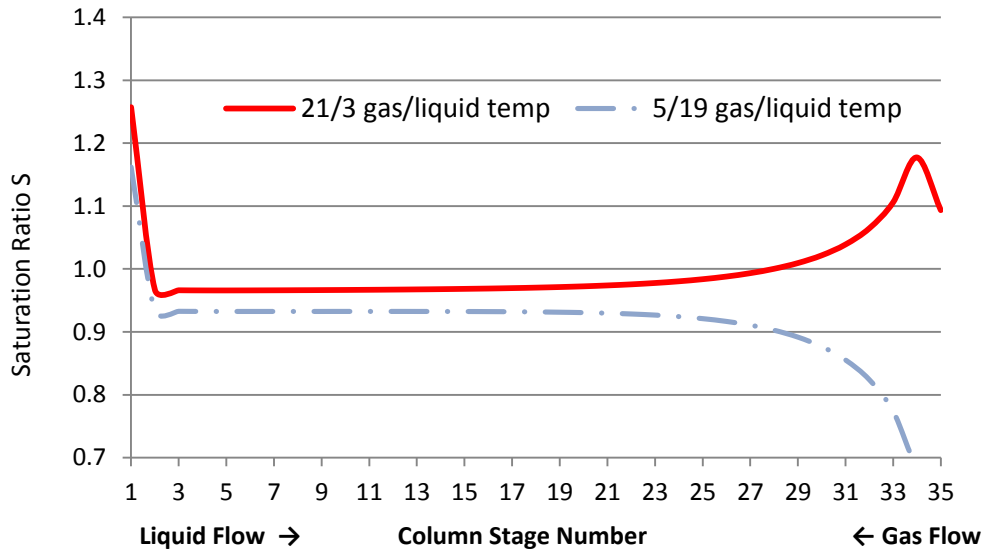


Figure 36 – Effect of gas and liquid temperatures on saturation ratio

#### 4.1.6 System Pressure

Figure 37 & 38 show the effect of varying system pressure on percent NO<sub>x</sub> removal and saturation ratio. Lower pressure tends to increase the saturation ratio, although the change over the pressures tested did not significantly change the portion of the column over  $S_{crit}$ . Percent NO<sub>x</sub> removal increases with increasing operating pressure.

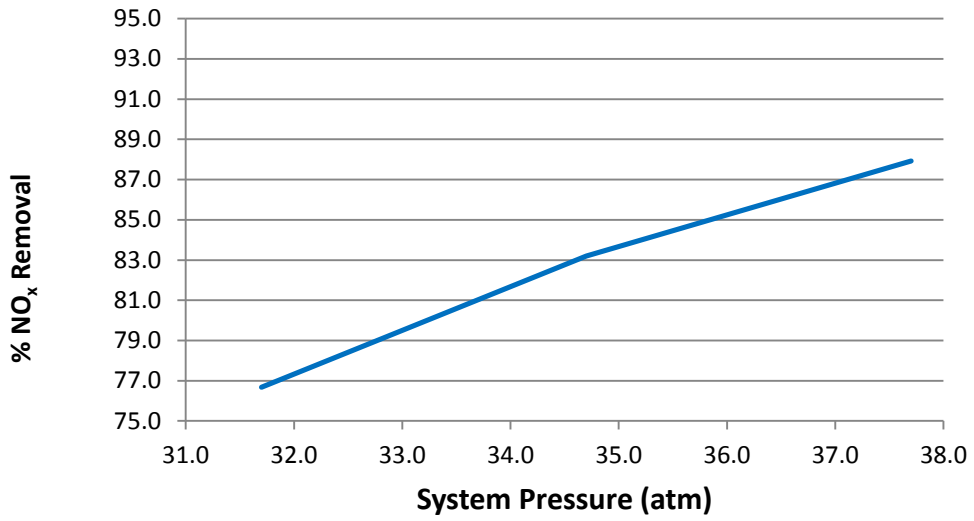


Figure 37 - % NO<sub>x</sub> removal vs. system pressure

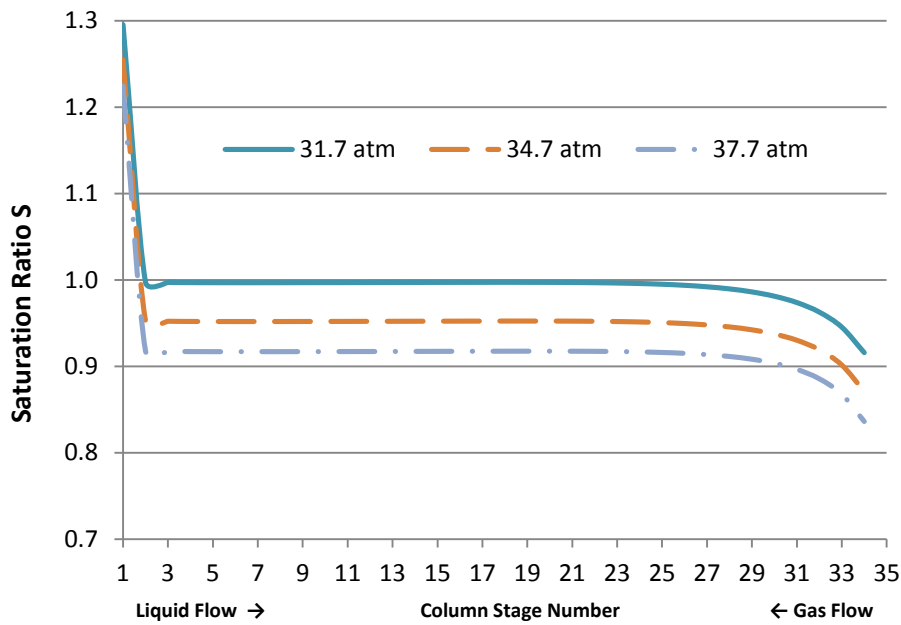


Figure 38 – Effect of system pressure on saturation ratio

## 5 Aerosol Effects

### 5.1 Availability of Condensable Vapor

The highlighted area of Figure 39 shows the areas where saturation ratio exceeds  $S_{crit} = 1.02$ . While aerosol size depends largely on the nuclei concentration  $C_n$ , the size can also be affected if there is a limited amount of condensable vapor. For the maximum case shown in Figure 39, the condensable mass was calculated using the simulated gas mole fractions, mole flow, and calculated equilibrium mole fraction of water. The condensable vapor was assumed to be the mass of water vapor available to bring the saturation ratio from  $S_n$  to  $S_{crit}$ .

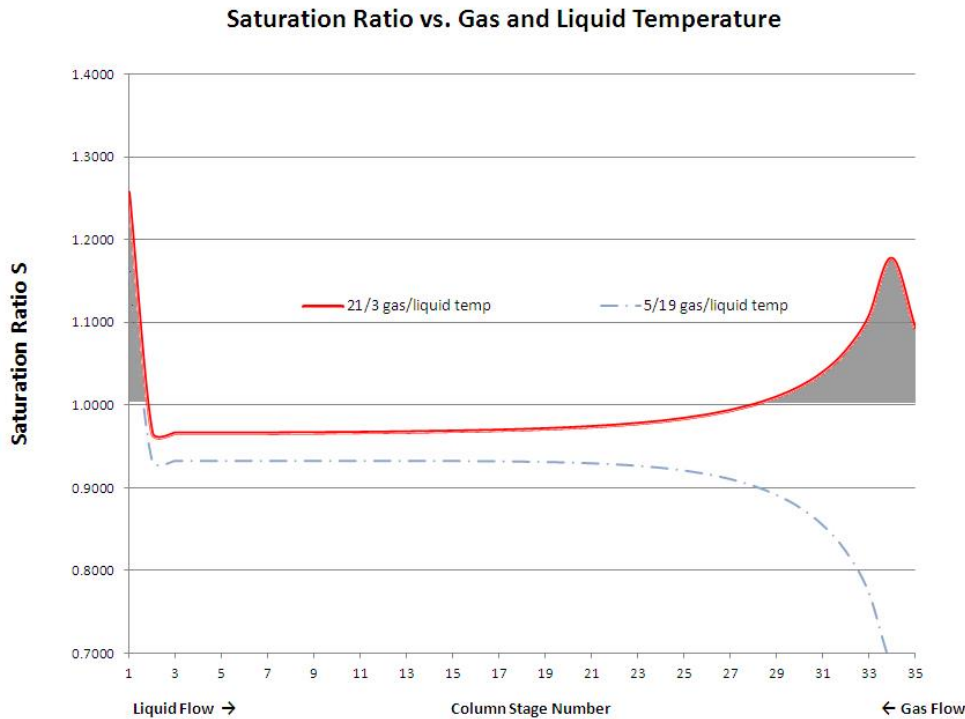


Figure 39 – Highlighted area on column saturation ratio profile showing areas where  $S > S_{crit}$ .

In the worst case scenario, total vapor available for condensation is shown in Table 14. For the base case, only the 1<sup>st</sup> stage exceeded  $S_{crit}$  as shown in Figure 39. However, even for this single stage, 12.49 kg/hr  $H_2O$  is available for condensation.



Stage	Mass available for aerosol formation kg/hr H <sub>2</sub> O
1	7.56
30	0.08
31	0.87
32	2.09
33	4.11
34	7.71
35	3.73
Total	26.14

Table 14 – Total water available for aerosol condensation above  $S_{crit}$  at 21 °C gas inlet and 3 °C liquid inlet temperatures.

## 5.2 Range of Estimated Aerosols

As reported above in Table 11 an estimate of aerosol nuclei characterization from an oxy fired boiler is  $C_N = 4.34 \times 10^6 \text{ particles/cm}^3$  with an average diameter  $D_N = 0.55 \mu\text{m}$ .

Droplet diameter  $d_{drop}$  can be estimated using Equation 46, with total liquid volume in a droplet  $V_{drop}$  calculated from equation 47

$$V_{drop} = \frac{4}{3}\pi \left[ \left( \frac{d_{drop}}{2} \right)^3 - \left( \frac{d_N}{2} \right)^3 \right] \quad (47)$$

and total mass of aerosol  $Q_a$  formed equal to:

$$Q_a = C_N \cdot V_{drop} \cdot v_g \cdot \rho_{H_2O} \quad (48)$$

Over a range of particle concentrations, aerosols show a maximum mass flow as shown in Figure 40. This graph assumes 1) that conditions exist in the column for the formation of aerosols and 2) that adequate condensable water vapor exists to support the calculated mass flow. Figure 40 does support the obvious conclusion that reducing particulate concentration at any level will reduce aerosol formation.

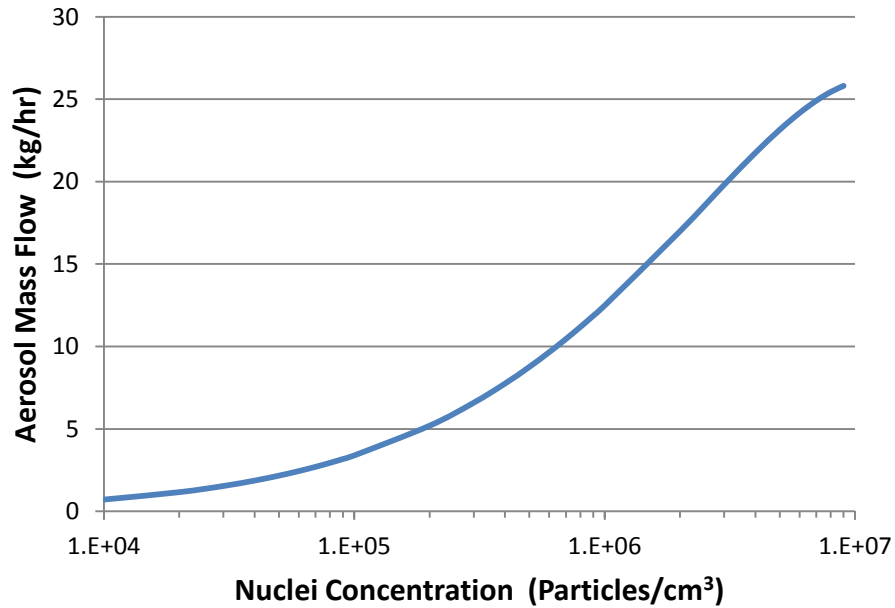


Figure 40 - Aerosol mass flow vs. entering nuclei concentration.

For simulation purposes orders of magnitude changes in particle concentration above and below the estimated concentration of  $C_N = 4.34 \times 10^6$  were used to estimate a maximum and minimum extent of potential aerosol formation up to the maximum presented in the data extracted from Ehrig [31] as shown in Table 15. It is important to note that the total potential aerosol liquid mass flow is in some cases higher than the available condensable vapor as calculated above, so the available vapor will be the determining factor affecting total aerosol mass under some operating conditions.

Nuclei concentration $C_n$ #/cm <sup>3</sup>	Droplet Diameter $d_{drop}$ μm	Droplet Liquid Volume $V_{drop}$ μm <sup>3</sup>	Total Aerosol Liquid Mass $Q_a$ kg/hr
4.34E+04	2.813	11.573	1.971
4.34E+05	2.100	4.761	8.109
4.34E+06	1.386	1.308	22.275
1.00E+07	1.128	0.664	26.042

Table 15 – Range of particle concentrations for simulation

### 5.3 Simulating Aerosol Equilibrium

Because of their small size, aerosols will quickly equilibrate with the surrounding gas. For example, Fulk [43] calculated that it takes only  $4.135 \times 10^{-10}$  seconds for a 3.26 μm diameter particle to reach equilibrium with CO<sub>2</sub> when transported in a concentrated gas. It can be assumed then that the aerosol droplets are in equilibrium with the surrounding gas and the concentration of gaseous species in the aerosol can be calculated by using known vapor liquid equilibrium data.

The NO<sub>x</sub> absorber Aspen model was modified in order to calculate the aerosol equilibrium concentration as model parameters are changed as shown in Figure 41.

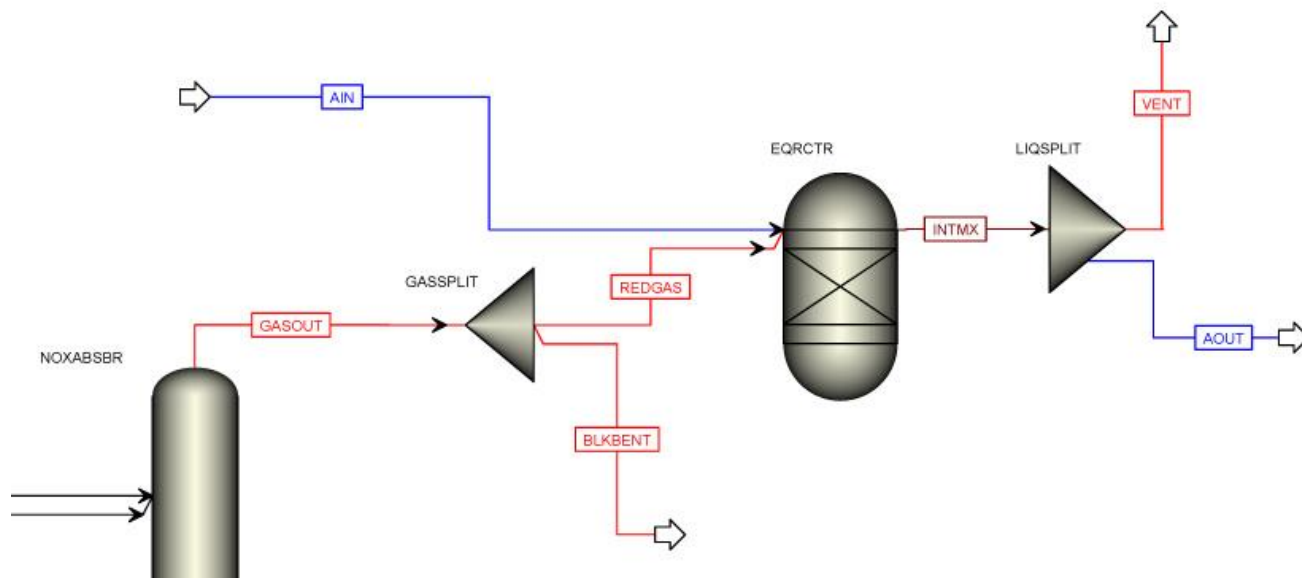


Figure 41 – Addition to Aspen NO<sub>x</sub> absorber model to calculate equilibrium concentrations in aerosols.

The exit gas from the NO<sub>x</sub> absorber was first split to reduce the total volume to more manageable levels, in this case 300 kg/hr (REDGAS stream). The reduced gas flow is combined with an amount of pure water (AIN stream) to achieve the required aerosol liquid mass fraction (AOUT stream) after reaching equilibrium.

The combined gas and aerosol liquid (INTMX stream) is fed into an Aspen equilibrium reactor block of sufficient size to allow full equilibrium to be achieved. The liquid phase reaction set was not included in this block because it is assumed that the bulk reactions in the NO<sub>x</sub> absorber have already taken place in both gas and liquid phase.

The product liquid (AOUT stream) was then separated as a dirty water split using an Aspen mixer block.

Results of the equilibrium for the base case simulation were compared with manual concentration calculations using the previously established Henry's law constants. The result of both methods shows good agreement as shown in Figure 42.

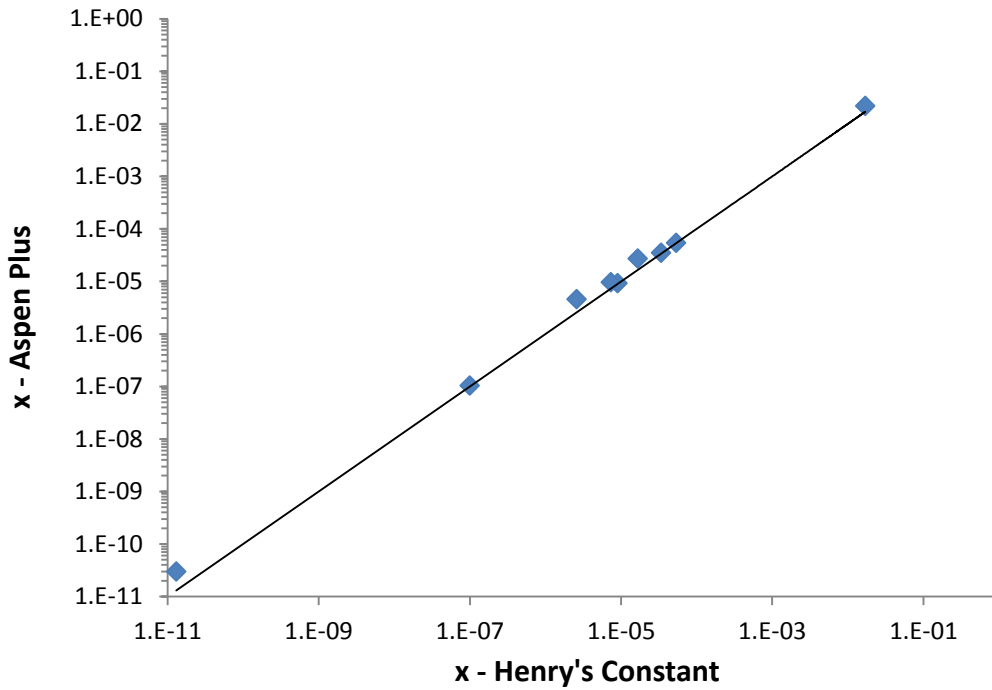


Figure 42 - Aerosol dissolved gas component mole fraction. Aspen results vs. calculated from Henry's constants.

#### 5.4 Aerosol emission estimates

The various scenarios of gas and liquid temperatures presented in Table 13 were simulated to estimate the effect of aerosols on emissions of the NO<sub>x</sub> absorber over the range of nuclei concentrations present in Table 15. The aerosol liquid mass was limited to a maximum of the available condensable water vapor above  $S_{crit}$  as described previously.

The available compounds simulated were grouped into four categories as shown in Table 16.

1	2	3	4
Total NO <sub>x</sub>	Other Condensable Nitrogen Components	Other Nitrogen Compounds in Solution	Other Non-Nitrogen Compounds
NO NO <sub>2</sub>	HNO <sub>3</sub> HNO <sub>2</sub> N <sub>2</sub> O <sub>3</sub> N <sub>2</sub> O <sub>4</sub>	N <sub>2</sub> N <sub>2</sub> O	CO <sub>2</sub> CO O <sub>2</sub> AR SO <sub>2</sub> SO <sub>3</sub> HCL H <sub>2</sub> SO <sub>4</sub>

Table 16 – Component categories in aerosol liquid

Total NO<sub>x</sub> transported with the aerosol will directly reduce the removal efficiency of the NO<sub>x</sub> absorber.

Condensable nitrogen components and other nitrogen compounds in solution may affect the total nitrogen removal of the process. In the case of an oxy-fired GPU, the nitrogen compounds in the liquid phase aerosols may not be efficiently removed in the later gas removal processes, resulting in a more contaminated CO<sub>2</sub> product.

The electrolytes in solution, both nitrogen and non-nitrogen containing, can also disassociate in water, reducing the pH which can cause corrosion or operating issues with downstream process such as heat exchangers and high pressure compressors that are not designed for low pH liquids. In these simulations, the resulting aerosol liquid ranged from 2 – 3 pH.

The base case Figure 43 shows the relative composition of the components in the aerosol produced. The colored bars correspond to the categories in Table 16.

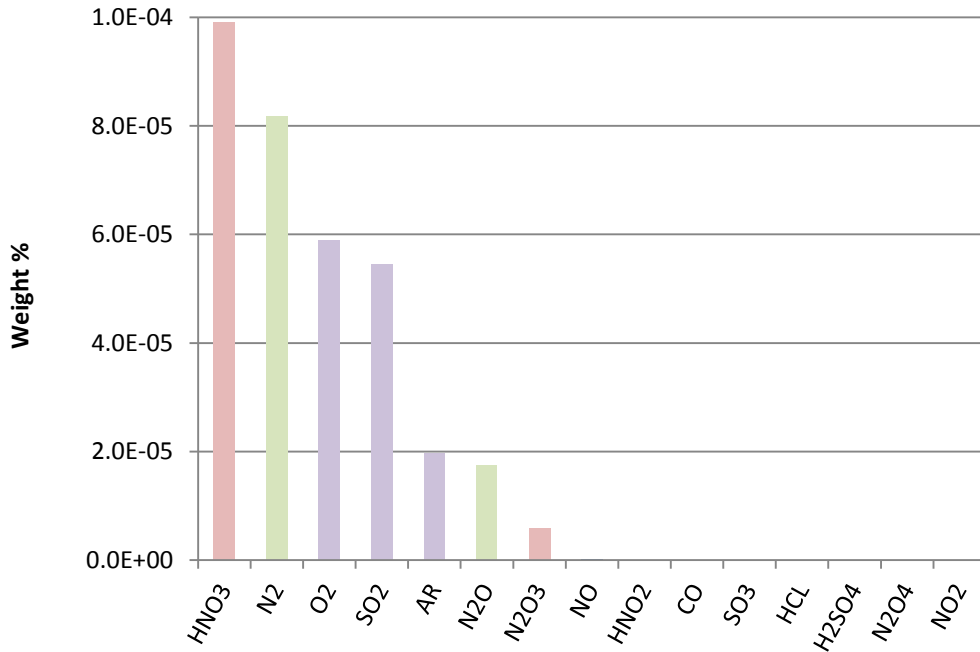


Figure 43 - Components dissolved in aerosol in base case. CO<sub>2</sub> (not shown) is the major component at .04 wt. percent.

Table 17 shows the detailed results of the simulation on the base case at four different nuclei concentrations. In this particular case, NO<sub>x</sub> emissions from the absorber (category 1) represent a tiny fraction of the NO<sub>x</sub> in the exit gas, less than 0.000016 % of the NO<sub>x</sub> emitted. So it is clear, strictly from the NO<sub>x</sub> removal perspective, that aerosols effects are insignificant in the modeled absorber.

Since NO<sub>x</sub> can react in solution to other components, the combination of component fractions 1 & 2 in solution can be important. Fractions 1 & 2 in the aerosol solution compose approximately 0.009 % of the total of these components exiting with the gas.

Nuclei concentration $C_n$	#/cm <sup>3</sup>	4.34E+04	4.34E+05	4.34E+06	1.00E+07
Total Aerosol Liquid Mass $Q_a$	kg/hr	1.971	8.109	12.490	12.490
Inlet Gas					
Total NO <sub>x</sub>	kg/hr	78.8	78.8	78.8	78.8
Other Condensible Nitrogen Components	kg/hr	0.0	0.0	0.0	0.0
Other Nitrogen Compounds in Solution	kg/hr	24,388	24,388	24,388	24,388
Other Non-Nitrogen Compounds	kg/hr	267,585	267,585	267,585	267,585
Outlet Gas					
Total NO <sub>x</sub>	kg/hr	13.2	13.2	13.2	13.2
Other Condensible Nitrogen Components	kg/hr	1.3	1.3	1.3	1.3
Other Noncondensable Nitrogen	kg/hr	24,373	24,373	24,373	24,373
Other Non-Nitrogen Compounds	kg/hr	261,006	261,006	261,006	261,006
Aerosol Liquid					
Total NO <sub>x</sub>	kg/hr	3.19E-07	1.31E-06	2.02E-06	2.02E-06
Other Condensible Nitrogen Components	kg/hr	1.26E-03	1.30E-03	1.31E-03	1.31E-03
Other Noncondensable Nitrogen	kg/hr	1.95E-04	8.04E-04	1.24E-03	1.24E-03
Other Non-Nitrogen Compounds	kg/hr	1.89E+00	7.78E+00	1.20E+01	1.20E+01

*Table 17 – Base case simulation results comparing composition of four component groupings to losses from dissolved components in aerosol at four different inlet nuclei concentrations.*

The effect of varying absorber conditions is shown in Figure 44. Two cases are shown in the chart compared to the base case. The 21-3 case represents the worst case scenario with maximum mass of aerosols emitted. In this case, gas temperature is high at 21<sup>o</sup>C, while absorber feed water temperature is low at 3<sup>o</sup>C. This scenario results in improved NO<sub>x</sub> removal, but significantly greater production of aerosols. The 2<sup>nd</sup> case presented 5-19 reduces gas temperature to 5<sup>o</sup>C but increases feed water temperature to 19<sup>o</sup>C.

Compared to the base case, increasing the top temperature of the absorber (5-19 case) increases the concentration of gas species in the aerosol and results in greater aerosol emissions per mass of aerosol. Decreasing the top temperature of the absorber (21-3 case) decreases solubility of the gas components as seen in the two left hand data points on the graph. However, the lower temperatures also increase the saturation ratio and results in more water vapor being available for condensation and formation of aerosols. The two right hand data



points show that the increase in aerosol formation eclipses the reduced solubility and actually increases nitrogen losses in the aerosol.

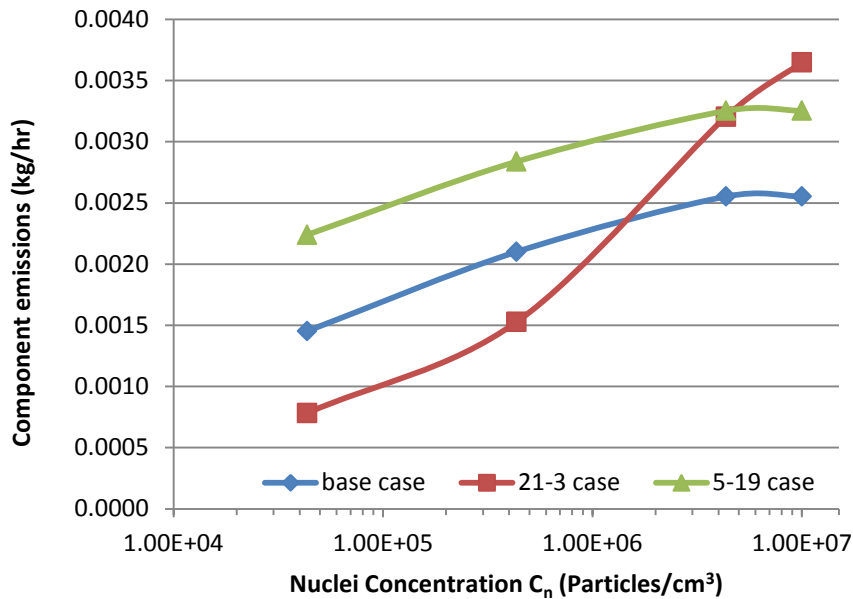


Figure 44 – Total nitrogen compounds emitted with aerosols at various absorber conditions

The results in Figure 44 were based on the assumption that the initial liquid in the aerosol (AIN stream to equilibrium reactor block EQRTR on Figure 41) to be pure water. The pure liquid is then equilibrated with the exit gas. In the 21-3 case, aerosols would be formed at the bottom of the column at the gas inlet, where the wash liquid has absorbed a considerable amount of the gas constituents, gas concentrations are high, and there is significant time for the liquid phase reactions shown in Table 5 to take place in the aerosols. These reactions produce compounds such as nitric acid in the water phase, that have relatively low vapor pressure at the temperatures and concentration simulated, and will tend not to dissipate.

To see the effect of this on the final aerosol composition, the aerosol input stream (AIN) was assumed be at the concentration shown in Table 18. This is the composition of a pure water stream feed into the absorber column at 21-3 case condition, at stage 35 at the bottom of the column. This liquid concentration is then equilibrated with the absorber exit gas in the EQRTR block. The result is a simulation representing the final concentration in aerosols when those aerosols are formed early in the absorber column.

Figure 45 show the results, compared to both the base case simulation and the 23-3 clean water case. The dirty water case emitted 2.3 times the total nitrogen of the corresponding clean water case. This suggests that aerosol emissions are affected by both the total liquid mass of aerosols formed and the location at which they are formed.

Component	AIN Mole Frac
CO <sub>2</sub>	2.1425E-02
H <sub>2</sub> O	9.7826E-01
O <sub>2</sub>	3.9021E-05
AR	1.0395E-05
N <sub>2</sub>	5.9447E-05
SO <sub>2</sub>	2.7495E-05
NO	2.6916E-05
HNO <sub>3</sub>	1.2532E-04
HNO <sub>2</sub>	1.1973E-05
H <sub>2</sub> SO <sub>4</sub>	3.5120E-18
N <sub>2</sub> O <sub>3</sub>	1.1970E-16
N <sub>2</sub> O <sub>4</sub>	1.4290E-12
NO <sub>2</sub>	1.7036E-22
N <sub>2</sub> O	9.1031E-06

*Table 18 – Water feed composition used in 21-3 contaminated water case simulation.*

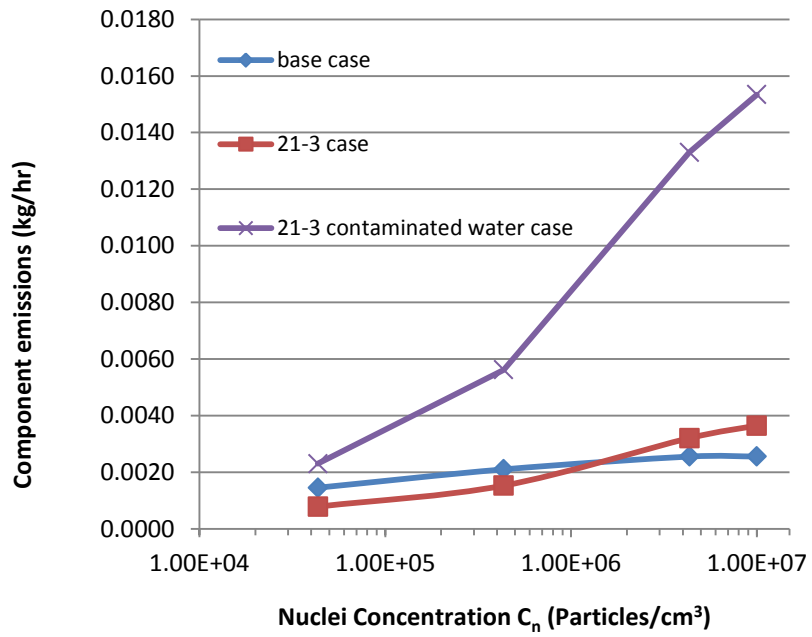


Figure 45 – Total nitrogen compounds emitted with aerosol in contaminated water case vs. base and 21-3 cases.

## 6 Conclusions

Aerosol formation through heterogeneous nucleation in aqueous gas absorption and the effect of these aerosols on final gas purity can be estimated using Aspen Plus. The most critical parameters for the analysis are inlet nuclei concentration and the saturation ratio profile through the absorber. With this information, the volume of the liquid aerosols exiting the absorber can be estimated. Composition of the aerosols can be estimated by equilibrating the liquid with the surrounding gas.

Of the various parameters affecting saturation ratio, absorber liquid inlet temperature has the greatest effect, with cooler liquid cooling the gas and creating an oversaturated situation. Since liquid inlet temperature is often lowered to improve absorber performance, it is important to note that the simultaneous increase in aerosol formation could have a detrimental effect.

Absorber pressure also has a similar effect, with increasing pressure improving NO<sub>x</sub> absorption, but also increasing the saturation ratio and the potential for aerosol formation.

When the conditions for aerosol formation are met, the total aerosol volume produced is affected by initial nuclei concentration and total vapor available above  $S_{crit}$ . In addition, the location where aerosols are formed can affect the final concentration of constituents in the aerosols as they exit the absorber.

## 7 References

1. White V, Allam R. Purification of Oxyfuel-derived CO<sub>2</sub> for Sequestration for EOR. In: Greenhouse Gas Control Technologies. Proceedings of the eighth international conference on greenhouse gas control technologies, 2006, pp.1-6
2. Kühnemuth, D., Normann, F., Johnsson, F., Andersson, K., Evaluation of Concepts for Secondary SO<sub>x</sub> and NO<sub>x</sub> Removal from the Oxy-Fuel Process, Proceeding of the 15th International Conference on the Properties of Water and Steam, Berlin, 2008.
3. Shabunya S., Wende B., Fisenko S., Schaber K., Simulations and Experiments of the Formation of Ammonium Chloride Particles in Wet Scrubbers, Chemical Engineering and Processing, 2003, 42, pp. 789-800
4. Radian International LLC, FGD Wet Scrubber Performance at High Flue Gas Velocities, EPRI Environmental Control Technology Center report TR-107131, November 1996
5. Counce, R. M. and Perona, J. J., Scrubbing of Gaseous Nitrogen Oxides in Packed Towersè AIChE J., 29,1983, pp. 26–32
6. Norman, F., Andersson, K., Leckner, B., Johnsson, F., Emission Control of Nitrogen Oxides in the Oxy-fuel Process, Progress in Energy and Combustion Science, vol. 35, issue 5, 2009, pp. 385-397
7. Joshi, J., Mahajani, V., Juvekar, V., Invited Review Absorption of NO<sub>x</sub> Gases, Chemical Engineering Communications, vol. 33, 1985, Issue 1-4,
8. Tsukahara, H., Ishida, T., Mayumi, M., Gas-Phase Oxidation of Nitric Oxide: Chemical Kinetics and Rate Constant, Nitric Oxide, vol. 3, issue 3, June 1999, pp. 191-198
9. Thiemann, M., Scheibler, E. and Wiegand, K., Nitric Acid, Nitrous Acid, and Nitrogen Oxides. Ullmann's Encyclopedia of Industrial Chemistry, 2000
10. Suchak, N., Jethani, K., Joshi, J., Modeling and Simulation of NO<sub>x</sub> Absorption in Pilot-Scale Packed Columns, AIChE Journal,1991, vol. 37, no. 3, pp. 323-339
11. Patwardhan, M., Pradhan, J., Joshi, J., Simulation of NO<sub>x</sub> Gas Absorption Under Adiabatic Condition and Comparison with Plant Data, Chem. Eng. Sci., 2002, 57, pp. 4831-4844
12. Green, D., Perry, R., Perry's Chemical Engineers' Handbook (8th Edition), 2008, McGraw-Hill.
13. Tsang, W., Herron, J., Chemical Kinetic Data Base for Propellant Combustion I. Reactions Involving NO, NO<sub>2</sub>, HNO, HNO<sub>2</sub>, HCN and N<sub>2</sub>O, J. Phys. Chem. Ref. Data 20, 609, 1991
14. Hoftyzer, P., Kwanten, J., Absorption of Nitrous Gasses, Part B, Processes for Air Pollution Control, CRC Press, 1972

15. Siddiqi, M., Petersen, J., Lucas, K., Influence of Nitrogen Monoxide on the Complex Phase and Chemical Equilibria in Wet Flue gas Cleaning Processes, *Ind. Eng. Res.*, 2003, 42, pp. 1406- 1413
16. Komiyama, H., Inoue, H., 20 Absorption of Nitrogen Oxides into Water, *Chemical Engineering Science*, vol. 35,1980, issue 1–2, pp. 154-161
17. Kenig, E., Kucka, L., Górak, A., Rigorous Modeling of Reactive Absorption Processes. *Chem. Eng. Technology*, 2003, 26: pp. 631–646
18. Hüpen, B., Kenig, E., Rigorous Modeling of NO<sub>x</sub> Absorption in Tray and Packed Columns, *Chemical Eng. Sci.*, 60, 2005, pp. 6462-6471
19. England, E., Corcoran, W., Kinetics and Mechanisms of the Gas-Phase Reaction of Water Vapor and Nitrogen Dioxide, *Industrial & Engineering Chemistry Fundamentals* 1974 13 (4), pp. 373-384
20. Kenig, E., Seferlis, P., Modeling Reactive Absorption, *Chemical Engineering Progress*, January 2009, pp. 65-73
21. Mertes, S., Wahner, A., Uptake of Nitrogen Dioxide and Nitrous Acid on Aqueous Surfaces, , *The Journal of Physical Chemistry* 99, (38),1995, pp. 14000-14006
22. Sander, R.: Compilation of Henry's Law Constants for Inorganic and Organic Species of Potential Importance in Environmental Chemistry, (version 3), Max-Planck Institute of Chemistry, 1999, [http://www.mpch-mainz.mpg.de/\\_sander/res/henry.html](http://www.mpch-mainz.mpg.de/_sander/res/henry.html)
23. Loutet K., Machecha-Botero A., Boyd T., Buchi S., Reid D., Brereton C., Experimental Measurements and Mass Transfer / Reaction Modeling for and Industrial NO<sub>x</sub> Absorption Process, *Ind. Eng. Chem. Res.* 2011, 50, pp. 2192-2203
24. Schaber K. Aerosol Formation in Absorption Processes, *Chemical Engineering Science*, 1995, 50-8, pp. 1347-1360
25. Gretscher H., Schaber K., Aerosol formation by heterogeneous nucleation in wet scrubbing processes, *Chemical Engineering and Processing*, 1999, 38, pp. 541-548
26. Hidy G., *Aersols: An industrial and environmental science*, 1984, Academic Press
27. Körber J., Schaber K., Modeling of heat and mass transfer with fog formation, *Heat and Mass transfer 1994: Proceedings of the Tenth International Heat Transfer Conference*, Brighton, UK, vol. 3, pp. 341-346
28. Weast R, *Handbook of Chemistry and Physics*, CRC Press, Cleveland, 1976
29. Hamill P., The Time Dependent growth of H<sub>2</sub>O-H<sub>2</sub>SO<sub>4</sub> Aerosols by Heteromolecular condensation, *Journal of Aerosol Science*, 1975, 6, pp. 475-482

30. Wix A., Schaber K., Ofenloch O., Ehrig R., Deudlhard P. Simulation of Aerosol Formation in Gas-Liquid Contact Devices, *Chem. Eng. Comm.*, 2007, 194, pp. 565-577
31. Ehrig R., Ofenloch O., Schaber K., Deuffhard P., Modeling and Simulation of Aerosol Formation by Heterogeneous Nucleation in Gas-Liquid Contact Devices, *Chemical Engineering Science*, 2002, 57, pp. 1151-1163
32. Fletcher N, Size Effect in Heterogeneous Nucleation, *J. Chem. Phys.*, 1958, 29, 572
33. Morris W., Yu D., Wendt J., Soot, Unburned Carbon and Ultrafine Particles Emissions from Air- and Oxy-Coal Flames, *Proceedings of the Combustion Institute*, vol.33, issue2, 2011, pp. 3415-3421
34. Gladney E., Small J., Gordon G., Zoller W., Composition and Size Distribution of In-Stack Particulate Material at a Coal-Fired Power Plant, *Atmospheric Environment*, 1976, 10:pp. 1071-1077
35. Schaber K., Körber J., Formation of Aerosols in Absorption Processes for Exhaust Gas Purification, *Journal of Aerosol Science*, 1991, 22, Suppl.1:S501-S504
36. Meij R., Winkel H., The Emissions and Environmental Impact of PM 10 and Trace Elements from a Modern Coal-Fired Power Plant Equipped with ESP and Wet FGD, *Fuel Processing Technology*, 2004, 85:641– 656
37. McElroy M., Carr R., Ensor D., Markowski G., Size Distribution of Fine Particles from Coal Combustion, *Science, New Series*, 1982, vol. 215, No. 4528: pp. 13-19
38. Adriano D., Page A., Elseewi A., Change A., Straughan I., Utilization and Disposal of Fly Ash and Other Coal Residues in Terrestrial Ecosystems: A Review, *Journal of Environmental Quality*, 1980, vol.9, No. 3:333-343
39. Wang H., Song Q., Yao Q., Chen C., Experimental Study on Removal Effect of Wet Flue Gas Desulfurization System on Fine Particles from a Coal-Fired Power Plant, *Proceedings of Chinese Society for Electrical Engineering*, 2008, vol. 8, No. 5:27-33
40. Yan J., Yang L., Bao J., Jiang A., Huang Y., Shen X., Impact Property on Fine Particles From Coal Combustion in Ammonia, 2009, *Proceedings of Chinese Society for Electrical Engineering*, 29(5) 21-26
41. Mirabel P., Clavelin J., Experimental Study of Nucleation in Binary Mixtures: The Nitric Acid–Water and Sulfuric Acid–Water Systems, *J. Chem. Phys.*, 1978, 68: 5020
42. Schaber K., Körber J., Ofenlock O., Deuffhard P., Aerosol Formation in Gas –Liquid Contact Devices – Nucleation, Growth and Particle Dynamics, *Chemical Engineering Science*, 2002, 57: pp. 4345-4356
43. Fulk S., Aerosol and Volatile Emission Control in CO2 Capture, Quarterly Report for January 1 – March 31, University of Texas at Austin, April 30, 2012

## 8 Appendix

### Appendix A – Example of calculation method

Below is an example of a typical calculation method that would be used for an actual running industrial gas absorption process. It is assumed that a suitable Aspen simulation model is available for the process.

#### Step 1 - Calculation of Saturation Ratio

Three pieces of data are required for the saturation ratio calculation: stage temperature, stage concentration of condensable components, and equilibrium concentration of those components.

Absorber column stage temperatures are available on the TPFQ tab under the RadFrac block using the following path in the Aspen data browser:

BLOCKS > ABSORBER > PROFILES > TPFQ

The highlighted results shown below can be brought into an Excel spreadsheet by cutting and pasting or by importing into Excel using the Aspen Simulation Workbook add-in.



TPFQ							
Compositions		K-Values		Hydraulics		Reactions	
Efficiencies		Properties		Key			
View: Summary		Basis: Mole					
Profiles							
Stage	Liquid temperature	Vapor temperature	Pressure	Heat duty	Liquid flow	Vapor flow	
	K	K	atm	cal/sec	kmol/hr	kmol/hr	
1	290.483681	290.483681	34.7	0	8252.53216	6877.19097	▲
2	290.50146	290.523917	34.7	0	8252.84888	7018.86612	
3	290.513668	290.534978	34.7	0	8252.98686	7019.18824	
4	290.523673	290.545083	34.7	0	8253.05127	7019.34134	
5	290.532945	290.555044	34.7	0	8253.08312	7019.42218	
6	290.542118	290.565226	34.7	0	8253.09962	7019.47138	
7	290.551487	290.575812	34.7	0	8253.10809	7019.50622	
8	290.561207	290.586916	34.7	0	8253.11163	7019.5341	
9	290.571375	290.59862	34.7	0	8253.11156	7019.55821	
10	290.582064	290.610995	34.7	0	8253.10843	7019.57998	
11	290.593336	290.624109	34.7	0	8253.10248	7019.60007	▼

Figure A.1 – Stage temperature data in Aspen

Absorber column stage vapor compositions (Figure A.2) are available on the Compositions tab under the RadFrac block using the following path in the Aspen data browser:

BLOCKS > ABSORBER > PROFILES > COMPOSITIONS

Composition of all components in the vapor phase is available. Only condensable components under the stated conditions with concentrations suitable for condensation aerosols need to be imported. In many cases water vapor will be the only significant condensing component.

TPFQ Compositions K-Values Hydraulics Reactions Efficiencies Properties					
View:		Vapor		Basis: Mole	
Composition profiles					
Stage	CO2	H2O	O2	AR	N2
1	0.82741258	0.00053754	0.03654349	0.00919280	0.12572021
2	0.83073871	0.00053879	0.03584574	0.00901789	0.12324581
3	0.83073851	0.00053914	0.03584502	0.00901736	0.12323948
4	0.83073385	0.00053944	0.03584546	0.00901711	0.12323649
5	0.83072727	0.00053973	0.03584644	0.00901699	0.12323492
6	0.83071988	0.00054003	0.03584772	0.00901691	0.12323399
7	0.83071214	0.00054033	0.03584917	0.00901686	0.12323334
8	0.83070424	0.00054065	0.03585078	0.00901682	0.12323283
9	0.83069622	0.00054098	0.03585251	0.00901679	0.12323239
10	0.83068808	0.00054133	0.03585438	0.00901676	0.12323199
11	0.83067979	0.00054171	0.03585639	0.00901673	0.12323163
12	0.83067132	0.00054210	0.03585854	0.00901670	0.12323129

Figure A.2 – Stage composition data in Aspen

The equilibrium vapor concentration of the condensing components selected can be obtained through the literature or using the aspen PL vapor pressure property available under the Aspen tools menu:

TOOLS > ANALYSIS > PROPERTY > PURE

An example of the Aspen property input screen is shown in Figure A.3. The output data (Figure A.4) can then be plotted in Excel and a best fit equation generated relating stage temperature to partial pressure of the components.

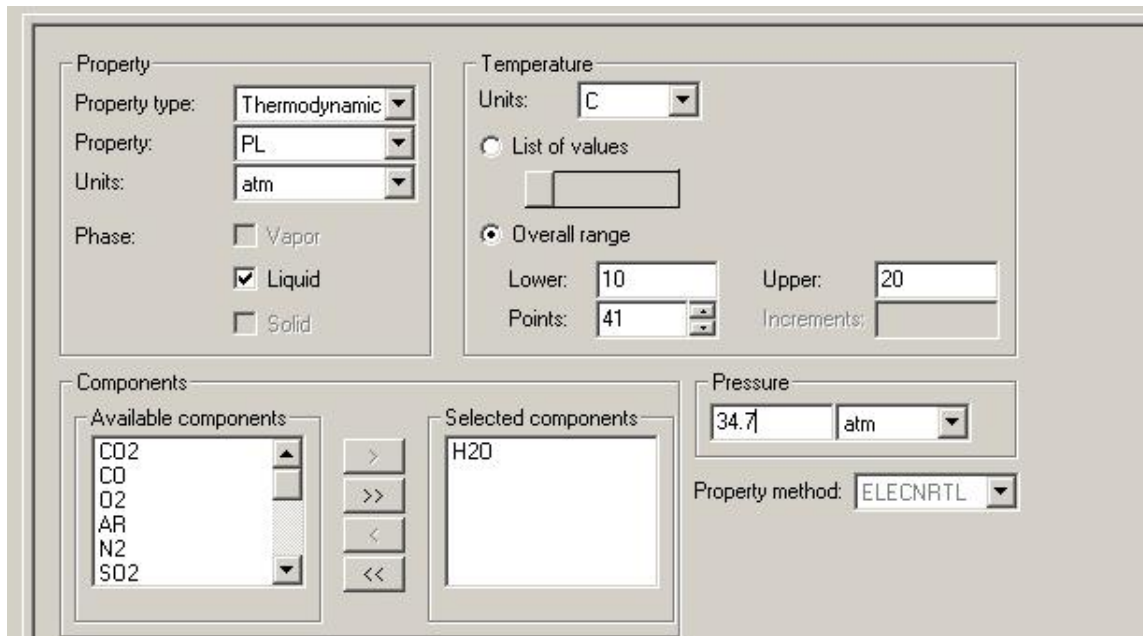


Figure A.3 – Aspen binary property input screen

Pure component properties analysis results

TEMP	PRES	LIQUID PL H2O
C	atm	atm
10	34.7	0.0121869
10.25	34.7	0.0123924
10.5	34.7	0.012601
10.75	34.7	0.0128127
11	34.7	0.0130275
11.25	34.7	0.0132454
11.5	34.7	0.0134666
11.75	34.7	0.013691
12	34.7	0.0139187
12.25	34.7	0.0141497
12.5	34.7	0.014384
12.75	34.7	0.0146218

Plot Wizard      Close

Figure A.4 – Vapor pressure data in Aspen

An example of the Excel spreadsheet showing stage equations is shown in Figure A.5.

Aspen data					Calculated		
	M	N	O	P	Q	R	S
1	Stage	Liquid Temp	Vap Temp	Mole Frac	Eq Pressure	PP	S
2	#	C	C	H2O	Water	Water	Water
3	1	3.000008	8.963126	3.2278E-04	0.00894	0.0112	1.2571
4	2	8.918393	8.974628	3.2379E-04	0.01163	0.011235	0.9668
5	3	8.940342	8.984553	3.2402E-04	0.01164	0.011244	0.9661
6	4	8.953944	8.994163	3.2421E-04	0.01165	0.01125	0.9659
				439E-04	0.01166	0.011256	0.9659
				457E-04	0.01167	0.011263	0.9660
				476E-04	0.01167	0.011269	0.9661
				496E-04	0.01168	0.011276	0.9663
				518E-04	0.01168	0.011284	0.9664
12	10	9.009877	9.066319	3.2542E-04	0.01169	0.011292	0.9667
13	11	9.020769	9.08272	3.2567E-04	0.01170	0.011301	0.9669
14	12	9.032629	9.101014	3.2596E-04	0.01171	0.011311	0.9672
15	13	9.045622	9.121558	3.2628E-04	0.01171	0.011322	0.9675
16	14	9.059937	9.144789	3.2663E-04	0.01172	0.011334	0.9679
17	15	9.075807	9.17125	3.2703E-04	0.01173	0.011348	0.9684
				3.2743E-04	0.01175	0.011364	0.9689
				3.2783E-04	0.01176	0.011382	0.9696
				3.2823E-04	0.01178	0.011402	0.9703
				3.2863E-04	0.01179	0.011426	0.9713
				3.2903E-04	0.01181	0.011454	0.9724
23	21	9.220091	9.4303	3.3103E-04	0.01184	0.011487	0.9738
24	22	9.26485	9.53167	3.3216E-04	0.01186	0.011526	0.9756
25	23	9.311589	9.63005	3.3352E-04	0.01189	0.011573	0.9777
26	24	9.366961	9.749782	3.3515E-04	0.01193	0.01163	0.9804
27	25	9.433055	9.896401	3.3715E-04	0.01198	0.011699	0.9837
28	26	9.512527	10.07698	3.3960E-04	0.01203	0.011784	0.9880
29	27	9.608751	10.30058	3.4264E-04	0.01210	0.011889	0.9933
				3.4568E-04	0.01219	0.012022	1.0003
				3.4872E-04	0.01229	0.012189	1.0094
				3.5176E-04	0.01242	0.012405	1.0217
				3.5480E-04	0.01258	0.012688	1.0389
				3.5784E-04	0.01279	0.013073	1.0647
35	33	10.8648	13.43683	3.9230E-04	0.01306	0.01362	1.1060
36	34	11.31548	14.51559	4.1630E-04	0.01341	0.014446	1.1773
37	35	11.85652	21.00001	4.5499E-04	0.01387	0.015788	1.0934
38	Gas Inlet					0.015164	

Equilibrium partial pressure =  
 $0.000034631 \cdot N_4^2 + 0.000042224 \cdot N_4 + 0.008499$   
 (Equation generated from Aspen vapor pressure data)

Partial pressure on stage  
 = mole fraction of component \* stage or column  
 pressure =  $P_{14} \cdot 34.7$

S ratio calculated using Equation 45 = partial  
 pressure from previous gas path stage /  
 equilibrium partial pressure =  $R_{27}/Q_{26}$

Note manual input of the partial pressure of the gas at inlet  
 conditions is required to calculate gas inlet stage S ratio

Figure A.5 – Excel spreadsheet showing example calculations for saturation ratio

## Step 2 - Calculate Droplet Mass

Ideally the concentration of particulate on the inlet gas is known from actual process measurements. It is important that these measurements include ultrafine particulate in the 0.1 - 1  $\mu\text{m}$  size range. If the particle concentration is not known then the steps shown in Figure 18 can be used as a rough estimate of particles entering the process. For the purposes of this example an inlet concentration of  $C_N = 4.34 \times 10^6$  particles/ $\text{cm}^3$  with a particle diameter of  $D_N = 0.55 \mu\text{m}$  is assumed.

Droplet diameter is estimated using equation 46:

$$\begin{aligned} D (\mu\text{m}) &= -0.3099 \ln(C_N) + 6.1226 \\ &= -0.3099 \ln(4.34 \times 10^6) + 6.1226 \\ &= 1.38 \mu\text{m} \end{aligned}$$

Droplet volume is calculated using equation 47:

$$\begin{aligned} V_{drop} &= \frac{4}{3}\pi \left[ \left( \frac{D_{drop}}{2} \right)^3 - \left( \frac{D_N}{2} \right)^3 \right] \\ &= \frac{4}{3}\pi \left[ \left( \frac{1.38}{2} \right)^3 - \left( \frac{0.55}{2} \right)^3 \right] \\ &= 1.29 \mu\text{m}^3/\text{droplet} \end{aligned}$$

Total aerosol mass is calculated from equation 48. In this example gas volume entering the column  $v_g = 66.5 \text{ m}^3/\text{min}$  and the density of water is  $\rho_{H_2O} = 0.99938 \text{ g/cm}^3$ .  $6 \times 10^{-8}$  is the sum of all unit conversions in the calculation below.

$$\begin{aligned} Q_a &= C_N \cdot V_{drop} \cdot v_g \cdot \rho_{H_2O} \\ &= 4.34 \times 10^6 \times 1.29 \times 66.5 \times 0.99938 \times 6 \times 10^{-8} \\ &= 22.3 \text{ kg/hr} \end{aligned}$$

22.3 kg/hr is the maximum aerosol mass available. As explained in section 5.1 the available condensable components above  $S_{crit}$  may limit the amount of aerosol that can form. The maximum vapor available for condensation on each stage can be calculated using equation A-1. Gas molar flow rate is available from the Aspen results table. In this example a gas molar flow rate of 7044 kmoles/hr was used. 1.02 is  $S_{crit}$  and 18.01528 is the molecular weight of water.

Available condensable vapor

$$= \left( \frac{(p_{i_{n+1}} - (p_{i_n}^{eq} \cdot 1.02))}{P} \right) \cdot \text{gas molar flow(kmoles/hr)} \cdot 18.01528$$

Equation A-1 – Available Condensable Vapor

Figure A.6 shows this calculation applied to the data from Figure A.5. The result is a total of 17.5 kg/hr of condensable water available in the column for aerosol formation.

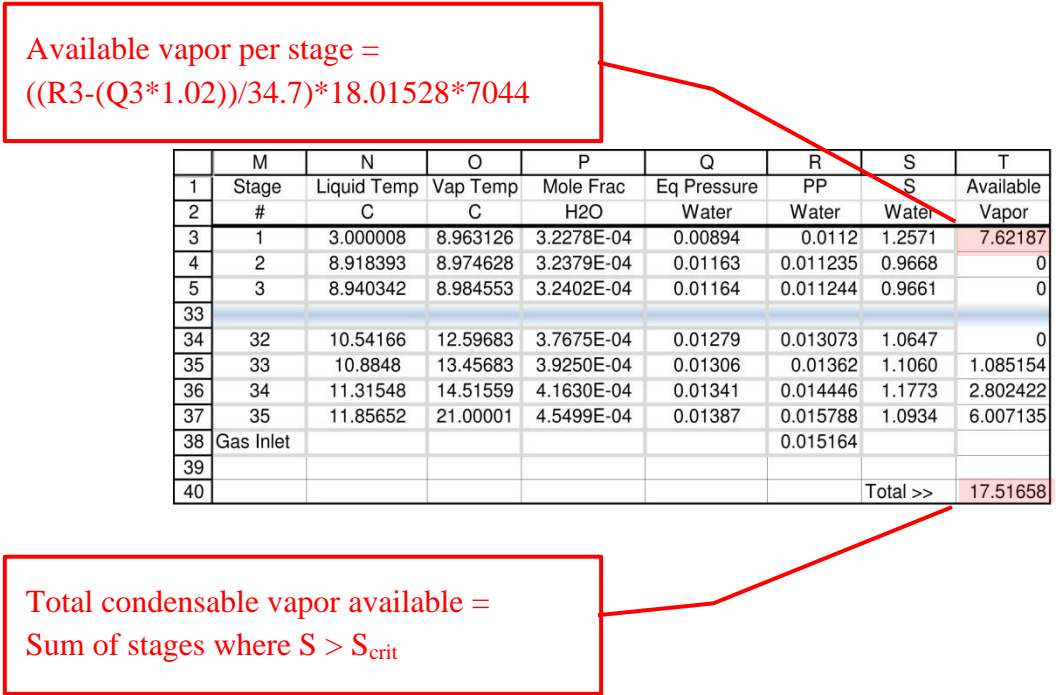


Figure A.6 – Excel spreadsheet showing available vapor calculations

Since the available vapor at 17.5 kg/hour is less than the potential aerosol mass of 22.3 kg/hour calculated above, the smaller number is used for aerosol mass in the simulator. This mass of aerosol can then be equilibrated with the gas phase as described in section 5.3 to determine the total emissions due to aerosols.